Composite Structures 290 (2022) 115538

Contents lists available at ScienceDirect

Composite Structures

journal homepage: www.elsevier.com/locate/compstruct

Meso-scale Finite Element (FE) modelling of biaxial carbon fibre non-crimp-fabric (NCF) based composites under uniaxial tension and in-plane shear

Han Yin *, Qianqian Li, Lorenzo Iannucci

Department of Aeronautics, Imperial College London, Exhibition Road, London SW7 2AZ, UK

ARTICLE INFO

Keywords:
Non-crimp fabric (NCF)
Polymer-matrix composites
Meso-modelling
Finite element analysis (FEA)

ABSTRACT

Non-crimp-fabrics (NCF) are promising materials in aerospace applications. The complex internal structure of NCF composites could influence the in-plane performances, which needs to be comprehensively studied. The novel three-dimensional (3D) *meso*-scale repeated unit cell (RUC) models were proposed for biaxial NCF composites based on the Finite Element (FE) method to conduct a systematic parameter study, including layup sequence, out-of-plane tow waviness, resin-rich areas, transverse tow placements and delamination. The meso RUC model could effectively predict the homogenised uniaxial tensile and in-plane shear properties of biaxial NCF composites based on their *meso*-scale constituent and material properties. A multiscale framework was also developed for biaxial NCF composites. A micromechanical representative volume element (RVE) model provided homogenised mechanical properties for tows, and a macroscopical FE model validated the test results using the homogenised results obtained from meso RUC models. The numerical results were in good agreement with the experiment results. Therefore, the multiscale framework provides an insight into the critical parameters influencing the in-plane properties of NCF composites and an analysis tool for NCF material design.

1. Introduction

The NCF blanket consists of fabric layers in specific orientations stitched together with through-the-thickness polyester yarns [1]. NCF materials are easy-handling, cost-saving, and permeable [2]. The resin transfer moulding (RTM) process offers a cost-effective solution to manufacture NCF composites with a high fibre volume fraction, complex shape, and good surface quality. The NCF composites manufactured by the RTM process enable the mass production of composite structural components applied in automotive, aerospace, marine and energy [2]. Due to the potential value in the aerospace industry, NCF materials are expected to become the primary materials of aircraft wings [3]. Therefore, it is worth investigating and improving the mechanical properties of NCF composites.

NCF composites consisting of fibre tows and resin-rich areas were reported to have heterogeneous structures at *meso*-scale [4–8]. The tows in NCF composites have slightly crimp in the out-of-plane direction, caused by the combined effects, including neighbouring plies, stitch tension and compaction [1,9,10]. The out-of-plane tow waviness could cause the reduction of the compressive strength of NCF composites [8]. Diamond-shaped resin-rich areas caused by stitching yarns in NCF plies contributed to the decreases in tensile, in-plane shear and compressive strengths [11–13]. NCF composites were reported to have better interlaminar fracture toughness and damage tolerance than unidirectional laminates due to the reinforcement of stitching yarns and increased delamination path [8,11,13]. Nevertheless, the inferior in-plane strengths could limit the widespread application of NCF composites, and the critical factors influencing the in-plane strengths are still under investigation. A systematic study has not been conducted regarding the roles of structural characteristics and interlaminar strengths of NCF composites in determining their in-plane strengths.

Comprehensive studies [4–8,10,12,14] proposed RVE models based on the FE method to investigate the influences of geometrical and material nonlinearities on the stiffness [4–7,10,12] and strengths [8,14] of NCF composites. Digital image correlation measurements were used to generate full-field strain maps and validate the RVE results regarding damage initiation and progression in NCF composites [15–17]. The two-dimensional (2D) RVE models proposed in some studies [6–8,10,14] might not be able to reflect actual stress states in NCF composites. In this study, the novel 3D RVE models were proposed to capture more accurate

* Corresponding author.
E-mail address: han.yin16@imperial.ac.uk (H. Yin).

https://doi.org/10.1016/j.compstruct.2022.115538
Received 31 August 2021; Received in revised form 23 February 2022; Accepted 30 March 2022
Available online 1 April 2022

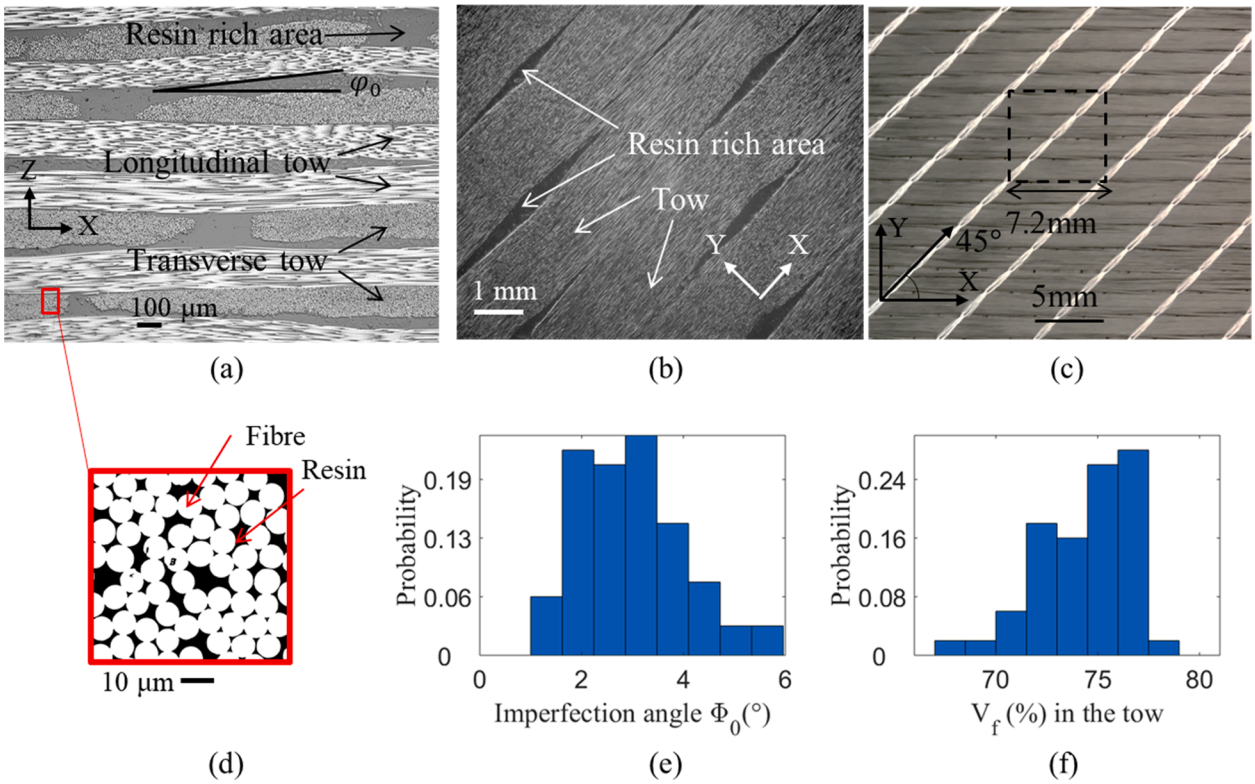

Fig. 1. The internal structure of the biaxial NCF composite: (a) An optical micrograph at the cross-sectional view; (b) An optical micrograph at the in-plane view; (c) The construction of the biaxial NCF material; (d) Cross-sectional view of the tow; (e) Distribution of the imperfection angle φ_0; (f) Distribution of fibre volume fraction in the tows V_f.

stress states in NCF composites. In addition, most studies mentioned above focused on predicting elastic modulus or investigating damage initiation. Few studies regarding predicting the tensile and in-plane shear strengths using RVE models have been conducted.

This study aimed to develop novel 3D RUC models for biaxial NCF composites to investigate how their structural characteristics and delamination influenced the uniaxial tensile and in-plane shear strengths. Experimental results provided geometrical parameters for the multiscale FE modelling. The stereo-digital image correlation (DIC) measurements generated full-field strain maps to validate the FE modelling. The FE analysis followed a hierarchical sequence from micro to macro to provide homogenised material properties at different scales. The homogenised results of micro RVE models could represent the properties of tow, which was shown in Appendix A and used as material inputs of meso RUC models. The homogenised results of meso RUC models were used as material inputs of the macroscopic damage model, which represented the cross-sectional properties of biaxial NCF composites. The study also successfully employed the user-defined material model (UMAT) developed by Iannucci et al. [18–20] to simulate the macroscopical damage of biaxial NCF composite in the uniaxial tensile and in-plane shear coupon tests.

2. Materials and experimental tests

2.1. Materials

The composite in this study was composed of carbon biaxial non-crimp fabric with an areal weight of 150 GSM per ply (Cristex Ltd, UK) and epoxy resin MTM57 (Solvay). The polyester yarns were stitched through the thickness and added an areal weight of 8 GSM to the biaxial NCF blanket. The fabric was composed of 12 K TORAY T700S carbon fibres. Biaxial NCF blankets were cut parallel to fibre directions to generate 0° and 90° plies. A total of 8 plies of biaxial NCF blankets were laid up with resin films, followed by autoclave fabrication. The nominal volume fraction of the NCF panel was 60%. Depending on the cutting direction, two layups of NCF composites were obtained for tensile tests: A $[0/90]_{4s}$ and B $[90/0]_{4s}$. The cutting direction was rotated by 45° to fabricate the in-plane shear specimens. The specimens were cut into 250 × 25 mm^2 using a waterjet cutter, with an average thickness of 2.4 mm ± 0.2 mm. End tabs were fabricated from woven glass fibre-reinforced polymer composites. The length and thickness of end tabs were chosen to be 50 mm and 1.5 mm, respectively. Therefore, the gauge lengths of the tension and in-plane shear specimens were both 150 mm.

2.2. Optical observation of the biaxial NCF composite

Fig. 1 (a) shows an optical microphotograph of the biaxial NCF composite at the cross-sectional view, which indicates that the NCF composite is composed of tows and resin-rich areas at *meso*-scale. Fig. 1 (b) shows the optical microphotograph of the NCF ply at the in-plane view, where through-thickness stitching yarns cause diamond-shaped resin-rich areas in the NCF plies and disturb fibre directions locally. The construction of the biaxial NCF material is presented in Fig. 1 (c), where the stitching direction is at the angle of 45° to the fibre direction. The minimum repeat unit of the NCF fabric based on the stitching gauge is 7.2 × 7.2 mm^2. The tow consists of fibre and matrix, based on the optical micrograph of the tow at the cross-sectional view, as shown in Fig. 1 (d).

According to previous studies [4–8,10–14], the tow imperfection angle φ_0 and fibre volume fraction V_f of the tows were important geometric parameters that controlled the mechanical behaviours of NCF composites. The distributions of the geometric parameters φ_0 and V_f are presented in Fig. 1 (e) and (f), respectively. The parameters were summarised from the optical micrographs taken from samples cut at different positions of the NCF panel. Using the ImageJ software, the imperfection angle φ_0 was calculated to be the maximum slope of the

Table 1
Young's modulus E_0, Poisson's ratio υ_{12} and tensile strength.

Layup	E_0 (GPa)	υ_{12}	Tensile strength (MPa)
layup A $[0/90]_{4s}$	70.7 ± 3.4	0.044 ± 0.014	1126.5 ± 63.5
layup B $[90/0]_{4s}$	68.6 ± 2.5	0.042 ± 0.006	1382.9 ± 35.4

Table 2
Shear modulus G_{12} and strength τ_{12}.

Shear modulus G_{12} (GPa)	Shear strength τ_{12} (MPa)
4.5 ± 0.1	98.3 ± 2.3

0° tows, and the fibre volume fraction of the tow V_f was calculated to be the areal fraction of the fibres in the cross-section of a tow. At least 50 data were summarised to present the distributions of each geometric parameter. The mean values and standard deviations of φ_0 and V_f were 3° ± 1° and 74% ± 2%, respectively.

2.3. Mechanical results of uniaxial tensile and in-plane shear tests

Uniaxial tensile and in-plane shear tests were carried out according to the standard ASTM D3039 [21] and D3518 [22], respectively. Tests were performed at a 2 mm/min loading rate on a servo-hydraulic Instron universal testing machine with a 250 kN loading capacity. With the 2-mm gauge length, biaxial strain gauges were attached to the surface of tensile and in-plane shear specimens within the gauge length to measure the longitudinal and transverse strains.

At least six repetitive tensile tests for the specimens with layups A and B were conducted, respectively. Young's modulus E_0 and Poisson's ratio υ_{12} were calculated based on the longitudinal strain between 0.1 and 0.3%. The mechanical parameters E_0, υ_{12} and tensile strengths are summarised in Table 1. The tensile strengths measured in this study were slightly higher than the values provided in the FALCOM report [23], which stated the tensile strengths of biaxial NCF carbon fibre composites with a fibre volume fraction of 60% were between 800 and 1000 MPa. In addition, the tensile strengths of layups A and B have an obvious difference, which was explained in the simulation section.

At least three repetitive in-plane shear tests were conducted on the specimens with layups $[45/-45]_{4s}$ and $[-45/45]_{4s}$, respectively. The shear modulus G_{12} was calculated based on the shear strain between 0.2 and 0.4%. The layups did not cause an obvious difference in the shear test results. The averaged mechanical parameters G_{12} and shear strength are summarised in Table 2. The shear strength in this study was close to the values provided in the FALCOM report [23], which stated that the shear strengths of the biaxial carbon fibre NCF composites with a fibre volume fraction of 60% were between 80 and 90 MPa.

2.4. Post-mortem photographs

During the tensile tests, it was worth noting that the surface 0° tows debonded from the specimens with layup A $[0/90]_{4s}$ first, and then the final failure occurred. However, the final failure directly occurred in the specimens with layup B $[90/0]_{4s}$. The post-mortem photographs of the tensile and in-plane shear specimens are shown in Fig. 2 (a)-(c). An entire view of the specimen and a close-up of the failure zone are presented to characterise failure modes. In Fig. 2, X-axis and Y-axis represent fibre directions, and Z-axis represents the thickness direction, consistent with the axes marked in Fig. 1. The tensile specimens with layups A and B indicate a brittle failure mode [21,24] because a crack develops across the section within the gauge length. The crack propagates completely in the specimen with layup B. However, it can be found that the surface longitudinal tows debond from the specimen with layup A. The specimens with layup A had lower tensile strengths than those with layup B, which might be attributed to the debonded tows. The phenomenon is validated by the meso FE modelling in Section 3.2.2. Fig. 2 (c) shows the failure mode of the in-plane shear specimen. A significant softened area is generated due to the large shear deformation. The close-up view indicates that interlaminar failure is due to fibre rotation [25]. The role of interlaminar delamination on the in-plane shear strength is validated by the meso FE modelling in Section 3.3.3.

2.5. DIC measurements of uniaxial tensile and in-plane shear tests

Full-field strain measurements were recorded by the stereo-DIC (GOM, Germany) during uniaxial tensile and in-plane shear tests. Two cameras were used to monitor the deformation of the specimens. The measured volume of the sensor was 160 (length) × 135 (width) × 105 (depth) mm^3, and 2752 pixels × 2200 pixels were contained in an image. The strain maps were generated with the facet size of 17 pixels × 17 pixels and the point distance of 15 pixels. Therefore, the pixel size was around 0.06 mm.

Virtual strain gauges with the size of 7.2 mm, corresponding to the length of the unit cell for the biaxial NCF composite in Fig. 1 (c), were generated in DIC measurements using the GOM correlate software. The uniaxial tensile stress–strain curves measured by physical and virtual strains are compared in Fig. 3 (a). The results of physical and virtual strain gauges are close. For in-plane shear tests, as the applicable range

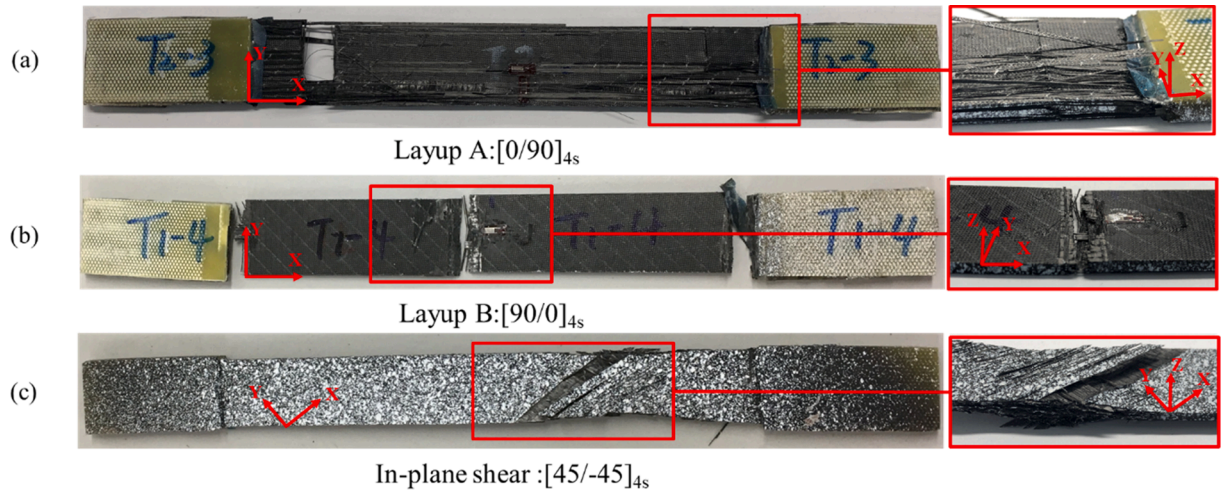

Fig. 2. Post-mortem photographs of test specimens: (a) A tensile specimen with layup A $[0/90]_{4s}$; (b) A tensile specimen with layup B $[90/0]_{4s}$; (c) An in-plane shear specimen with layup $[45/-45]_{4s}$.

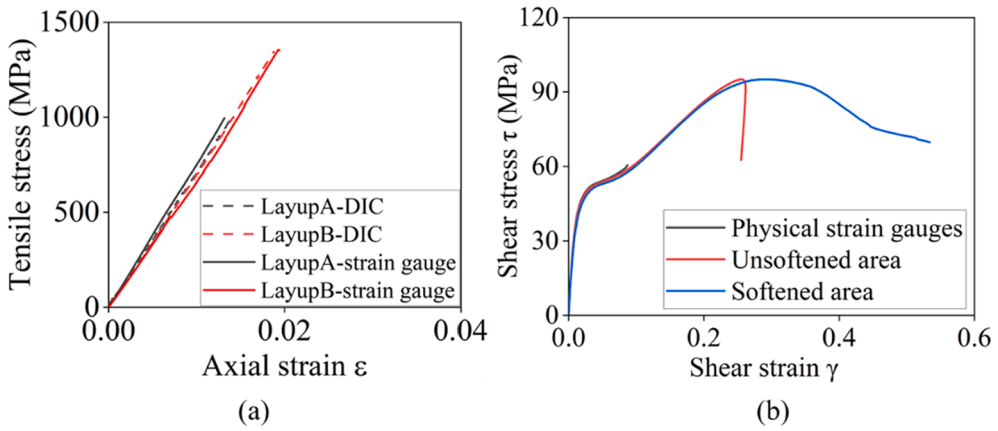

Fig. 3. Stress–strain curves measured by physical and virtual strain gauges: (a) Uniaxial tensile test; (b) In-plane shear test.

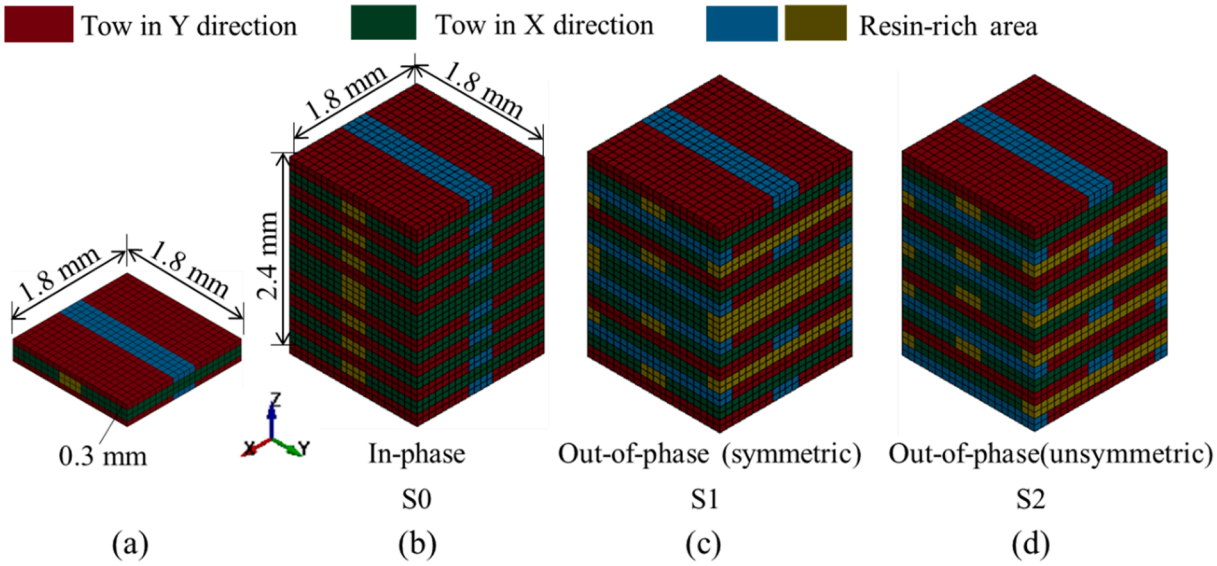

Fig. 4. The meso RUC models with different internal structures: (a) The minimum RUC model; (b) In-phase placed transverse tows S0; (c) Out-of-phase placed transverse tows (symmetric about the middle plane) S1; (d) Out-of-phase placed transverse tows (unsymmetric about the middle plane) S2.

of the physical strain gauges is between ± 0.045, only the virtual strain gauges can present the complete in-plane shear stress–strain curves, as shown in Fig. 3 (b). The strains of the non-softened and softened areas are both presented, and the maximum local shear strain of the NCF specimen is in the softened area. The influence of the DIC measurement uncertainty on the strain results is discussed in Appendix B.

3. Mesomechanical FE modelling

3.1. Model set up

As shown in Fig. 4, the RUC models consisting of tows and resin-rich areas represent internal structures of biaxial NCF composites. The tows are assumed to be perfectly straight and have a rectangular cross-section. The thickness of an NCF ply is calculated to be 0.15 mm, corresponding to the averaged ply thickness. The volume fraction of tow in the RUC model is 81%, based on the fibre volume fraction of 60% in the biaxial NCF composite and the local fibre volume fraction of 74% in the tows. As shown in Fig. 4, eight-node hexahedral solid elements with one-point integration are adopted in the meso RUC models. The mesh is about 0.08 mm. Two layers of elements are stacked in the thickness direction of the tow to capture the bending behaviour. The influence of the mesh size on the predicted results is discussed in Section 5.

Fig. 4 (a) represents the meso RUC model with a minimum size of 1.8 × 1.8 × 0.3 mm^3. According to the previous studies, the extreme placements of transverse tows in the internal structure of NCF composites included the in-phase and out-of-phase modes [10,26]. In addition to the in-phase placed transverse tows shown in Fig. 4 (b), this study proposes out-of-phase placed transverse tows symmetric or unsymmetric about the middle plane, as shown in Fig. 4 (c) and (d). For simplification, the structure with the in-phase placed transverse tows was named 'S0', and the structures with out-of-phase placed transverse tows symmetric and unsymmetric about the middle plane were named 'S1' and 'S2', respectively.

To investigate the influence of the RVE size, the minimum RUC model with the size of 1.8 × 1.8 × 0.3 mm^3 was used as a translational unit to generate models with the greater sizes, such as 3.6 × 3.6 × 0.3 mm^3, 5.4 × 5.4 × 0.3 mm^3, and 7.2 × 7.2 × 0.3 mm^3. Periodic boundary conditions (PBCs) were applied to the opposite faces of the meso RUC models to derive the equivalent stress and strain between the RUC and the homogenised internal structure of the biaxial NCF composite, following the method proposed in the relevant study [27]. In addition, the meso RUC models with the full-thickness of 2.4 mm (equal to the thickness of the tensile specimen) and different internal structures S0, S1 and S2 mentioned above were used to investigate the influences of free boundary and internal structure on the in-plane strengths. PBCs were

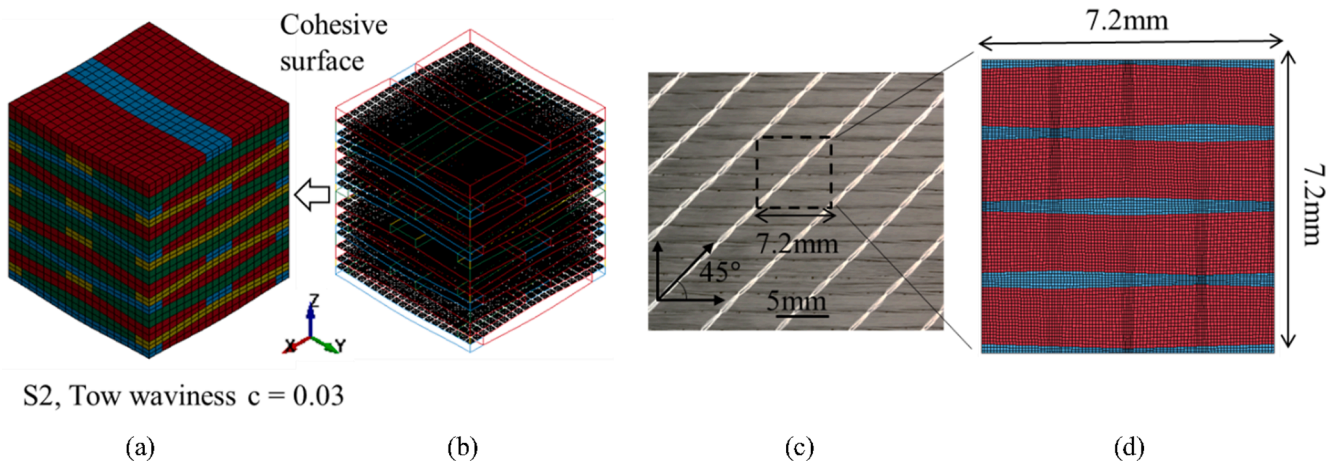

Fig. 5. (a) The S2 structure combined with tow waviness c = 0.03; (b) Cohesive surfaces for interlaminar delamination in the meso RUC model; (c) The minimum unit of the NCF fabric; (d) The schematic of the meso RUC model with diamond-shaped resin-rich areas.

applied on the opposite surfaces of the full-thickness RUC models except for their top and bottom surfaces.

Tow waviness was incorporated into some RUC models for a parameter study. As shown in Fig. 5 (a), tow waviness is introduced into the S2 structure of the biaxial NCF composite. The shape function of the out-of-plane tow waviness is assumed to be sinusoidal [28]:

$$z(x) = \left(a_1 + \frac{a_2}{2} - \frac{c}{2}\right) + \frac{c}{2}\cdot\cos\left(\frac{2\pi x}{\lambda}\right)$$

where a_1 and a_2 represent the thickness of 90° and 0° tows, respectively; λ is the nearest central distance between the cross-section of tows in the same layer; c/2 is the amplitude of tow waviness; z and x are the local coordinates in the thickness and longitudinal directions of the tow, respectively. In this study, a_1 and a_2 are equal to 0.15 mm, and λ is 1.8 mm. The parameters c = 0.01, 0.02, and 0.03 correspond to the maximum imperfection angle 1°, 2° and 3° in the tow, respectively.

Delamination was added to some RUC models for a parameter study. The cohesive surfaces are inserted at the interfaces between NCF plies by activating option 9 of tiebreak contact, as shown in Fig. 5 (b). The cohesive surface in LS-DYNA has been successfully employed to model delamination damage of laminates and fibre–matrix debonding [29–31]. The fracture model for the cohesive surface was developed from the mix-mode cohesive material model with the bilinear traction-separation law [32].

The normal stiffness in the contact was set to be $K = 10^5$ GPa/m for computational stability. According to the relevant studies [33,34], the normal stiffness for modelling the ply interface was between 10^5-10^7 GPa/m. The above values caused a difference of less than 1% in predicting tensile strengths in this study. Therefore, the value 10^5 GPa/m was applied to the interface between NCF plies. The higher value could increase the number of iterations and the difficulty to converge [35], which was not adopted in this study. As mode I fracture was hardly involved in the damage process of uniaxial tension and in-plane shear, the cohesive normal t_n^0 and shear t_s^0 strengths were assumed to be the same. The cohesive strengths of 40 MPa [14], 70 MPa [23] and ∞ (perfectly bonded) were employed in the parameter study. The normal Γ_I and shear Γ_{II} fracture energies of cohesive surfaces were assumed to be 100 J/m^2.

Polyester yarns were not directly modelled in the meso RUC models due to their minor contribution to the global stiffness of NCF composites [36]. The stitching yarns cause the generation of diamond-shaped resin-rich areas in NCF composites, as indicated in Fig. 1 (b). Therefore, the influence of diamond-shaped resin-rich areas on the tensile and in-plane shear strengths of the biaxial NCF composite was investigated. Fig. 5 (d) presents the meso RUC model with the diamond-shaped resin-rich areas, established according to the minimum unit of the NCF fabric shown in Fig. 5 (c).

The meso RUC model with diamond-shaped resin-rich areas was in the size of 7.2 × 7.2 × 0.3 mm^3, and the meso RUC model with channel-shaped resin-rich areas with the same size was chosen as the counterpart. The channel-shaped resin-rich areas had a width of 0.342 mm. Due to the lack of reliable statistics on the sizes of resin-rich areas, the maximum width of the diamond-shaped resin-rich areas was assumed to be 0.45 mm. Therefore, the minimum width was 0.234 mm, to keep the volume fraction of the tows in the meso RUC model with diamond-shaped and channel-shaped resin-rich areas consistent.

It should be noted that the out-of-plane tow waviness caused fibre undulation. The local material axis was defined in each element of tows so that the major direction was tangential to the sinusoidal shape function. Besides, uniaxial tensile strain ε_x and in-plane shear strains ε_{xy} were applied to the meso RUC models for different loading cases, respectively. The homogenised strain and stress were calculated based on the methods proposed in the relevant study [27].

3.2. Uniaxial tension

3.2.1. Material model

When the meso RUC model was subject to uniaxial tension, matrix and fibre tensile failures occurred in 90° and 0° tows, respectively. The tows in the meso RUC model have the same cross-section as unidirectional laminates and hence could be modelled by the built-in material model 54 for composite damage in LS-DYNA. The material model has the merit of simple parameters input and could predict composite failure modes, including matrix failure, fibre–matrix shearing, and fibre failure. Matrix cracking was implicitly modelled, and the stress degradation was not considered in the element of the 90° tow. The stress in the element of the 0° tow reduced to zero after reaching the fibre tensile strength, which causes the final collapse of the FE model.

The parameters of the tow used in the above material model were analysed with the micro RVE models as indicated in Appendix A, including elastic modulus and transverse tensile strength. The longitudinal and transverse tensile strengths of the tow with a fibre volume fraction of 74% were 3626 MPa and 87 MPa, respectively. The longitudinal tensile strength provided an upper limit for fibre tensile failure, estimated based on the rule-of-mixtures (ROM). The transverse tensile strength was derived by the micro RVE model with the interfacial strength of 80 MPa, assuming the interfacial strength was equal to the tensile strength of the epoxy resin. The relevant studies [37,38] have demonstrated that the Mohr-Coulomb yield criterion could be used to model the plasticity and pressure-dependent behaviour of epoxy resin.

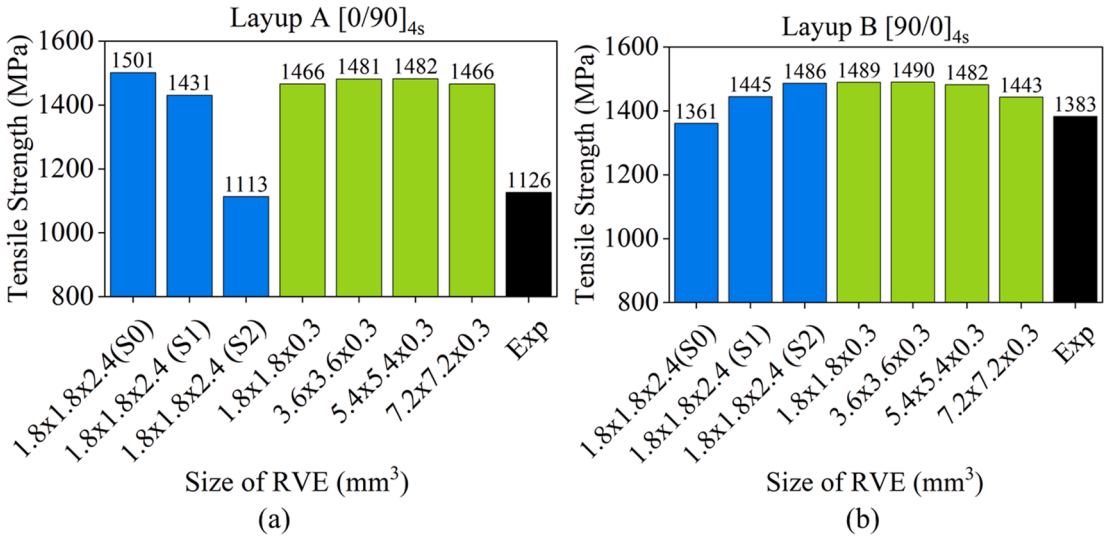

Fig. 6. The meso RUC models with different sizes and internal structures subject to uniaxial tension: (a) Tensile strengths of layup A; (b) Tensile strengths of layup B.

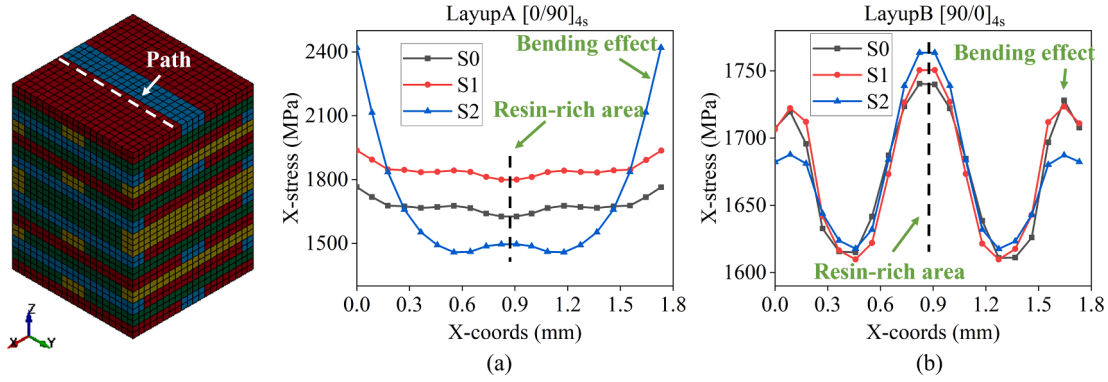

Fig. 7. The local X-stress distributions along a path in the longitudinal direction of the 0° tows in the meso RUC models under uniaxial tension with structures S0, S1 and S2 at applied strain ε = 0.01:(a) The surface 0° tows in the models with layup A; (b) The 0° tows below the surface 90° tows in the models with layup B.

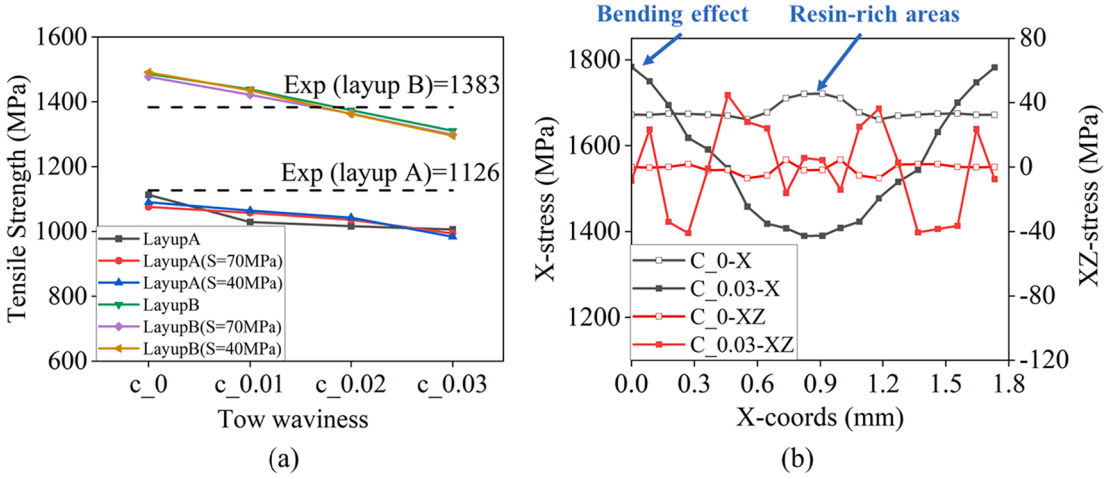

Fig. 8. The influence of tow waviness and interlaminar strength on the tensile strengths of the meso RUC models: (a) Tensile strength vs tow waviness of the models with the interlaminar shear strengths of 40 MPa, 70 MPa and ∞; (b) Local X- and XZ-stress distributions along a path in the longitudinal direction of the interior 0° tow in the models (layup B) with tow waviness c = 0 and 0.03 at the applied strain ε = 1%.

Therefore, the built-in material model 173 in LS-DYNA for the Mohr-Coulomb yield criterion was used to model the matrix [32]. The material parameters of the matrix are listed in Table A1 of Appendix A.

3.2.2. *Influence of RVE size and internal structure*

The meso RUC models with different sizes were constructed to investigate the influence of the RUC size on the tensile strength. The

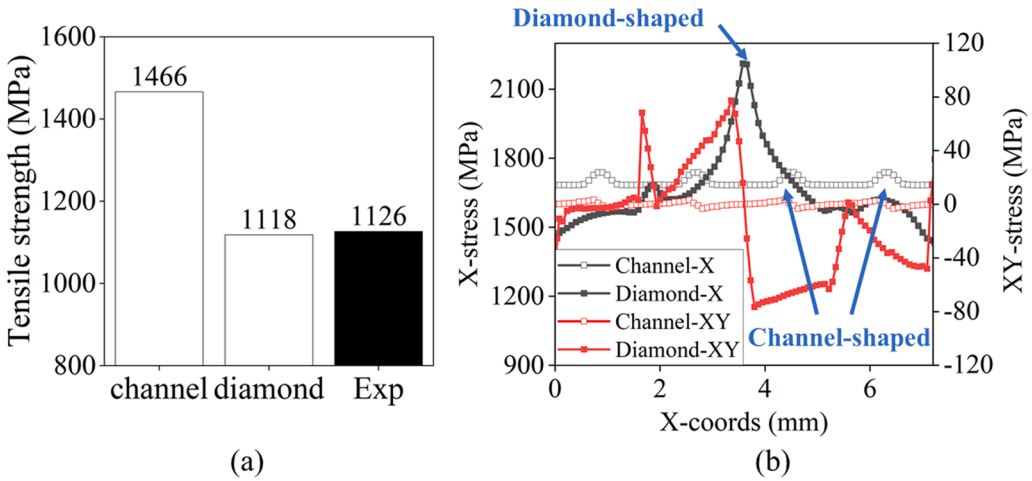

Fig. 9. The meso RUC models with the diamond and channel-shaped resin-rich areas under uniaxial tension: (a) Tensile strength; (b) Local X-stress and XY-stress distributions along a path in the longitudinal direction of the 0° tows in the meso RUC models at the applied strain ε = 1%.

effects of layups A $[0/90]_{4s}$ and B $[90/0]_{4s}$ were achieved by imposing tensile displacement in the Y- and X-directions, respectively. The tensile strengths of the meso RUC models are summarised in Fig. 6 (a) and (b). The results show that the tensile strengths are not influenced by the in-plane size of the RUC models due to the application of PBCs. However, the tensile strengths of full-thickness RUC models have an apparent difference. The difference was explained by the following stress analysis of the 0° tows in the full-thickness models.

Fig. 7 shows the local X-stress distributions along a path in the longitudinal direction of the 0° tows in full-thickness meso RUC models with internal structures S0, S1 and S2 at the applied strain ε = 1%. The path in the models with layup A is chosen from the surface 0° tow, as shown in Fig. 7. The path in the models with layup B is chosen from the 0° tow below surface 90° tow. The stress concentrations are generated due to several factors, including the bending effect, resin-rich areas and the unsymmetric structure. The reasons for the stress concentrations at different locations are shown in Fig. 7 (a) and (b).

Due to the free boundary, a significant bending effect was found in the surface 0° tows in the models with layup A. The bending effect caused the stress concentrations of the surface 0° tows in the models with layup A. The bending stresses of the surface 0° tows were increased in the unsymmetric S2 structure. The bending effect was constrained in the models with layup B due to the surface 90° tows. The stress concentrations in layup B were mainly caused by resin-rich areas. Therefore, the internal structures S0, S1 and S2 had a minor influence on the tensile strengths of the models with layup B.

Therefore, the meso RUC model with the characteristics of S2 structure and layup A simultaneously had the lowest tensile strength among all the full-thickness RUC models. The tensile strengths of layup B were mainly influenced by the stress concentrations caused by resin-rich areas. The bending effect in layup A caused higher stresses than the stress concentrations near resin-rich areas, leading to the significant reduction of tensile strengths with layup A in experimental results.

3.2.3. *Influence of tow waviness and delamination*

Fig. 8 (a) shows the influence of tow waviness and interlaminar strength on the tensile strength. The increase of tow waviness leads to the reduction in tensile strengths. However, the models with layup B have a greater reduction than those with layup A. The stress concentrations in the models with layup A were still dominated by the bending effect caused by the stretching of surface 0° tows. Fig. 8 (b) presents the local X- and XZ-stress distributions along a path in the longitudinal direction of interior 0° tows in the models with layup B. The local stresses in the models with tow waviness c = 0 and 0.03 are compared. It can be found that the maximum X-stresses are caused by the resin-rich areas in the model with c = 0, while the maximum X-stresses are caused by the bending effect of crimped tows in the model with c = 0.03. In addition, the XZ-stresses increase with tow waviness. Therefore, the increase of tow waviness had a more significant influence on the tensile strength of layup B than that of layup A. Interlaminar strengths had a minor influence on the tensile strengths because delamination was not involved in the damage process of uniaxial tension.

3.2.4. *Influence of the shape of resin-rich areas*

The comparison between the tensile strengths of the meso RUC models with the diamond-shaped and channel-shaped resin-rich areas is presented in Fig. 9 (a). The presence of diamond-shaped resin-rich areas causes a 24% reduction in the tensile strength. Fig. 9 (b) shows the local X- and XY-stress distributions along a path in the longitudinal direction of the 0° tows in the RUC models with diamond and channel-shaped resin-rich areas at the applied strain ε = 1%. The channel-shaped resin-rich areas cause minor stress concentrations. The X- and XY-stress concentrations are significant due to the diamond-shaped resin-rich areas, promoting the fibre tensile failure in the 0° tows.

3.3. *In-plane shear*

3.3.1. *Material model*

The 45° and −45° tows were subjected to the same shear deformation in the biaxial NCF composite under pure in-plane shear loading. Therefore, the material model 157 in LS-DYNA was used to model the nonlinear shear behaviours of the tows in the meso RUC model. According to the material model, the tows behaved elastically before reaching the yield strength and then presented nonlinear behaviour based on an effective plastic stress–strain curve. The brittle orthotropic Tsai-Wu failure criterion was combined with the anisotropic plastic material. The strength of 120 MPa, predicted by the micro RVE model with the interfacial strength of 100 MPa and a fibre volume fraction of 74%, was used in the material model as the maximum shear strength of the tow.

The in-plane shear stress–strain curve derived from the micro RVE model proposed in Appendix A was transferred to the effective plastic stress–strain curve as the input for the material model. With the pure shear boundary condition, stresses in the degree-of-freedoms except for XY were all in small magnitudes. Therefore, using the effective plastic stress–strain curve to describe the in-plane shear nonlinear behaviour of the tows was feasible in the current situation. Besides, the built-in material model 173 in LS-DYNA for the Mohr-Coulomb criterion was used to model the yielding and pressure-dependent behaviours of the matrix. The material parameters of the matrix are listed in Table A1 of Appendix A.

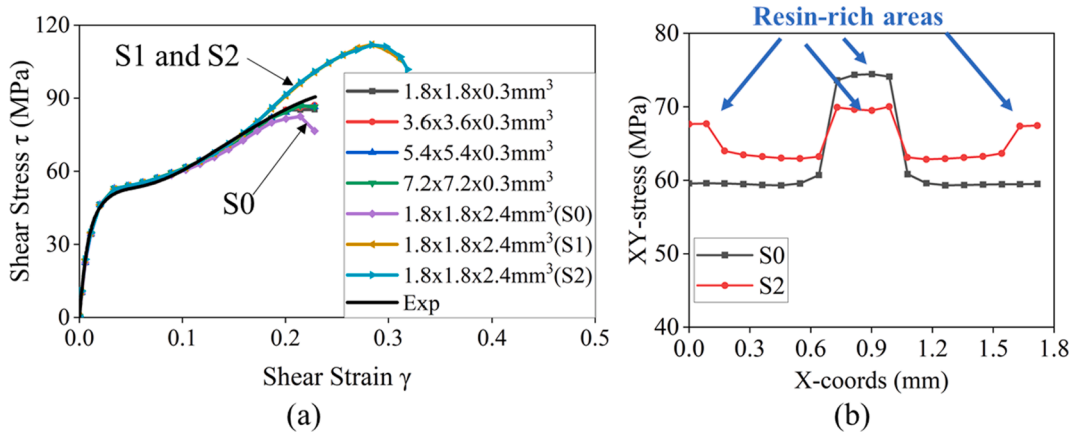

Fig. 10. The meso RUC models with different sizes and internal structures subject to in-plane shear: (a) In-plane stress–strain curves; (b) Local XY-stress distributions along a path in the longitudinal direction of the tows in the meso RUC models with S0 and S2 structures at the applied shear strain $\gamma = 10\%$.

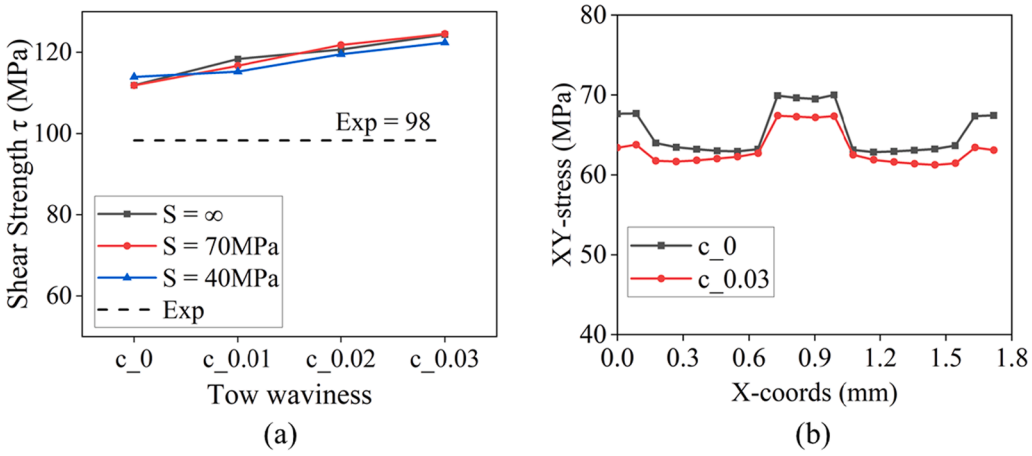

Fig. 11. The influence of tow waviness and interlaminar strength on the in-plane strengths of the meso RUC models: (a) In-plane shear strength vs tow waviness of the models with the interlaminar shear strengths of 40 MPa, 70 MPa and ∞; (b) Local XY-stress distributions along a path in the longitudinal direction of the tows in the models with tow waviness c = 0 and c = 0.03 at the applied shear strain $\gamma = 10\%$.

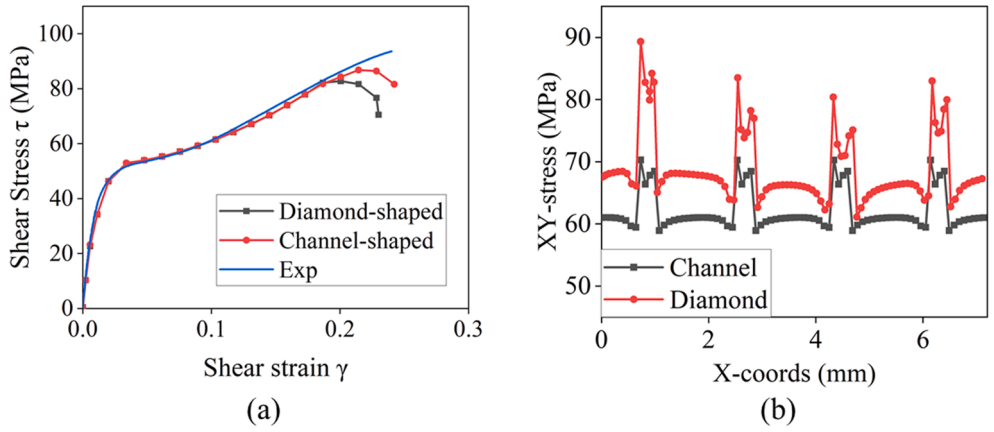

Fig. 12. The meso RUC models with diamond and channel-shaped resin-rich areas under in-plane shear: (a) In-plane shear stress–strain curves; (b) Local XY-stress distributions along a path in the longitudinal direction of the tows in the meso RUC models at the applied shear strain $\gamma = 10\%$.

3.3.2. Influence of RVE size and internal structure

The in-plane shear stress–strain curves of the meso RUC models with different sizes are depicted in Fig. 10 (a). The change of the in-plane sizes has a negligible influence on the shear responses. The full-thickness meso RUC models with S1 and S2 structures have higher in-plane shear strengths than the model with the S0 structure. Fig. 10 (b) compares the local XY-stress distributions along a path in the longitudinal direction of the tows in the models with S0 and S2 structures at the applied shear strain $\gamma = 10\%$, respectively. The maximum XY-stresses are reduced in the model with the S2 structure due to the dispersion

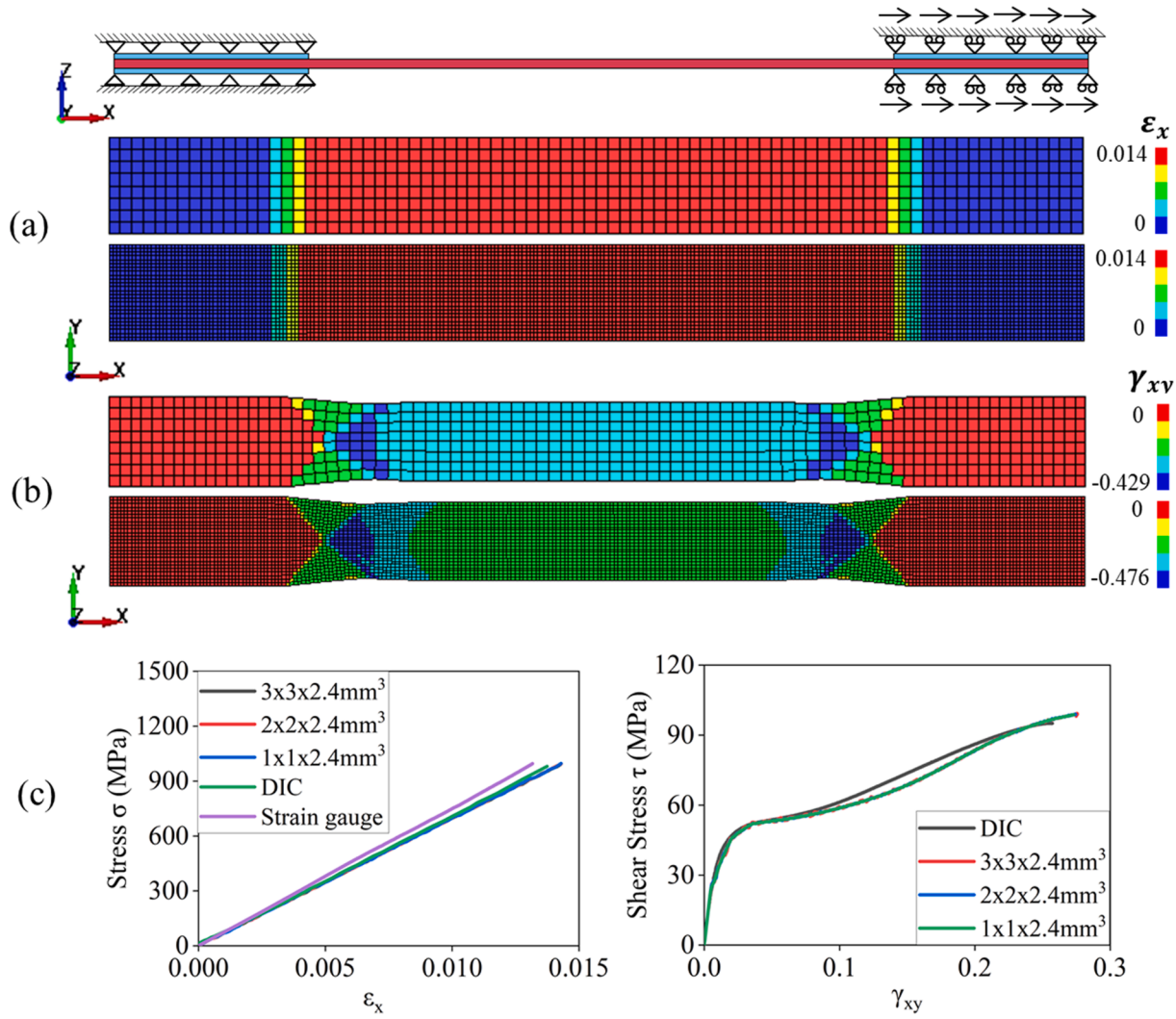

Fig. 13. FE modelling results of the biaxial NCF composite subject to uniaxial tension and in-plane shear: (a) Local strain ε_x in the tensile FE model at the applied tensile strain $\varepsilon = 1.4$ %; (b) Local shear strain γ_{xy} in the in-plane shear FE model at the applied shear strains $\gamma = 27\%$; (c) Stress–strain curves of uniaxial tension and in-plane shear FE modelling.

Table 3
Material properties of the biaxial NCF composite for numerical simulation.

Property	Values
Elastic properties	$E_x = 70\text{GPa}; E_y = 70\text{GPa}; G_{12} = 4.9\text{GPa}; \nu_{21} = 0.04$
Strength and failure strain	$\sigma_x = 1076\text{MPa}, \sigma_y = 1375\text{MPa}, \gamma_0 = 0.27, \gamma_{fail} = 0.6$
Intralaminar fracture toughness	$G_{x,f} = 80\ kN/m^2$, $G_{y,f} = 80\ kN/m^2$
Note	Layup A $[0/90]_{4s}$ was used

Table 4
FE modelling results of different mesh sizes.

Test type	Uniaxial tension		In-plane shear	
Mesh size (mm^3)	Failure strength σ (MPa)	Failure strain ε (%)	Failure strength τ (MPa)	Failure strain γ (%)
3 × 3 × 2.4	990.3	1.4	99.2	27.6
2 × 2 × 2.4	994.7	1.4	99.0	27.4
1 × 1 × 2.4	996.3	1.4	98.8	27.3
Difference	0.6%	0.2%	0.5%	0.9%

of resin-rich areas, leading to the higher shear strength.

The influence of layups $[45/-45]_{4s}$ and $[-45/45]_{4s}$ on the in-plane shear strength was negligible. The pure shear boundary conditions caused the equivalent shear deformations in all the layers of the biaxial NCF composites. The critical factor influencing the in-plane shear strength was the stress concentrations due to resin-rich areas.

3.3.3. *Influence of tow waviness and delamination*

Fig. 11 (a) shows the influences of tow waviness and the interlaminar strength on the in-plane shear strength. The increase of tow waviness improves the in-plane shear strength slightly, but the influence of interlaminar strength on the in-plane shear strength is negligible. Fig. 11 (b) presents the local XY-stress distributions along a path in the longitudinal direction of the tows in the models with waviness c = 0 and c = 0.03 at the applied shear strain γ = 10%. The increase of tow waviness contributes to reducing stress concentrations in the tows, leading to the higher in-plane shear strength.

Besides, the interlaminar strength of cohesive surfaces between NCF plies did not cause a significant influence on the in-plane shear strength because the major damage mechanism causing the nonlinear shear response was matrix plastic deformation of the tows. The meso RUC results showed that interlaminar delamination occurred when the tows reached the maximum shear strength. Hence, interlaminar delamination

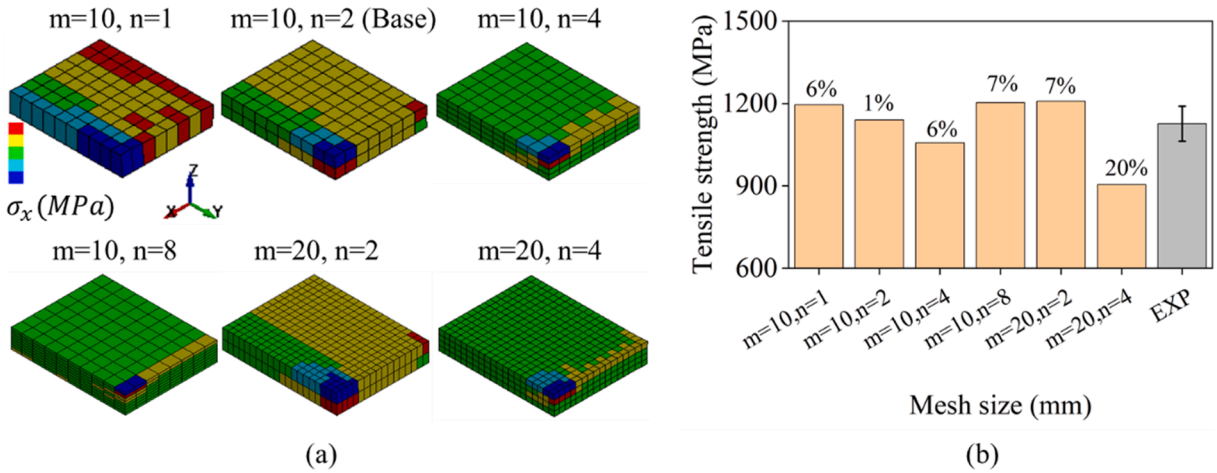

Fig. 14. The influence of the mesh size: (a) Local X-stress distributions in surface 0° tows of the meso RUC models with layup A at the applied strain ε = 0.01; (b) Tensile strengths of the models with layup A.

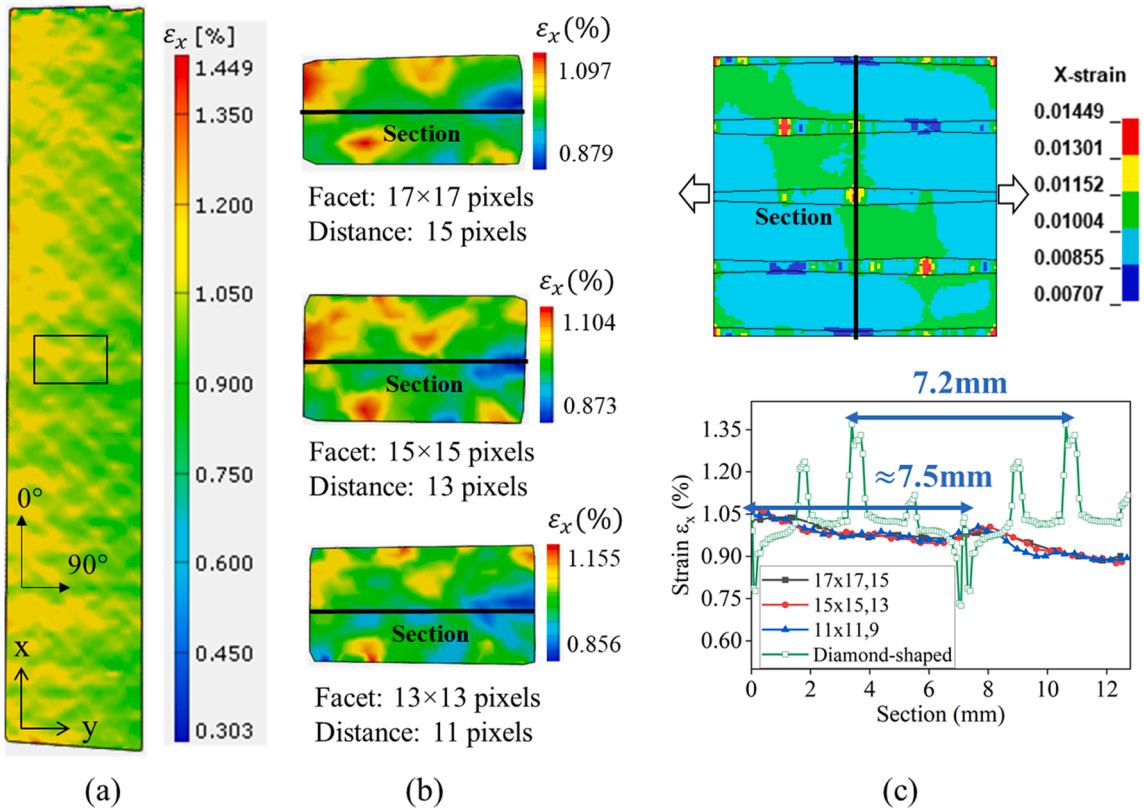

Fig. 15. The comparison between DIC measurements and the meso RUC model: (a) Strain map ε_x of the tensile specimen at the applied strain ε = 0.01 (facet size = 17 pixels, point distance = 15 pixels); (b) The local strain maps ε_x generated with different parameters; (c) Strain distribution ε_x along the sections in the meso RUC FE model and DIC measurements.

was not the dominating factor deciding the maximum shear strength of biaxial NCF composites.

3.3.4. *Influence of the shape of resin-rich areas*

The influence of diamond-shaped resin-rich areas on the in-plane shear strength was investigated. As shown in Fig. 12 (a), the stress–-strain curves indicate that the presence of diamond-shaped resin-rich areas causes the reduction in the in-plane shear strength of the meso RUC model. Fig. 12 (b) compares the local XY-stress distributions along a path in the longitudinal direction of the tows in the models with diamond-shaped and channel-shaped resin-rich areas at the applied shear strain γ = 10%. The diamond-shaped resin-rich areas cause higher XY-stresses, leading to the lower in-plane shear strength. However, a 4.7% reduction in the shear strength was slight, compared to a 24% reduction in the tensile strength.

4. FE modelling of coupon test

4.1. *Model set up*

The damage mechanics-based progressive damage model, proposed by Iannucci et al. [18–20] for woven carbon composites, has been

implemented in LS-DYNA for the shell element (plane stress) formulation. The damage was initiated with a strain-based approach and then developed following a fracture mechanics approach to avoid a mesh-dependent solution. The model described the macroscopical damage at the ply-level, including tensile and compression failure of fibre bundles in local warp and weft directions and in-plane shear damages. The accumulations of damages were defined with damage variables operating at the ply-level.

The damage model proposed above was used in this study to model the macroscopic damages of biaxial NCF composites. The cross-sectional properties of the biaxial NCF composite, including 0° and 90° NCF plies, were homogenised in an integration point. The thick shell element formulation was used to model the intralaminar damage of the biaxial NCF composite. A thick shell element could contain a different number of integrations, representing NCF plies with different fibre directions.

Fig. 13 (a) shows the boundary conditions in the FE modelling of uniaxial tension and in-plane shear tests. The boundary conditions are imposed on the surfaces of the end tabs. The Z-motion of the end tabs is constrained to model the clamping effect. The X-motion of the end tabs on the left side is constrained, and a prescribed X-motion is applied to the end tabs on the right side.

The material properties of biaxial NCF composites derived from the meso RUC model with tow waviness c = 0.03 are summarised in Table 3. The in-plane shear stress–strain curve derived from the meso RUC model was also used as a material input. The fracture toughness of the biaxial carbon fibre NCF composite G_f was estimated to be 80 kN/m^2, based on 160 kN/m^2 measured from the carbon fibre reinforced NCF laminate [39]. The fracture mechanics approach was also used to calculate in-plane shear failure. The shear strains $\gamma_0 = 0.27$ and $\gamma_{fail} = 0.6$ were used as initial and failure strains, respectively. The failure strain $\gamma_{fail} = 0.6$ was estimated from the softening area of the in-plane shear specimen by the DIC measurement.

4.2. FE modelling results

The maximum element size should be smaller than 5.7 mm due to the restriction of the characteristic element length l^* proposed in the study [20]. Therefore, different mesh sizes (1 × 1 × 2.4 mm^3, 2 × 2 × 2.4 mm^3 and 3 × 3 × 2.4 mm^3) were used in the tensile and in-plane shear FE models. The mesh size in the thickness direction was kept constant because the specimens were in 2D-stress states during tensile and in-plane shear tests. The shell element with multiple integrations could effectively model in-plane damages of the specimens. Stacking shell elements could cause redundant out-of-plane stresses. Fig. 13 (b) shows the local strain ε_x in the tensile specimen with the coarse (3 × 3 × 2.4 mm^3) and fine meshes (1 × 1 × 2.4 mm^3) at the applied strain ε = 1.4 %. It can be seen that the tensile strain ε_x is distributed uniformly within the gauge length, and the maximum tensile strains in the coarse and fine meshes are consistent. Fig. 13 (c) also compares the influence of coarse and fine meshes on the local strain γ_{xy} in the shear specimen at the applied strains γ = 27%. With the reduction of mesh size, the higher shear strain begins to be localised at the softened area. The uniaxial tensile and in-plane shear stress–strain curves are shown in Fig. 13 (c), indicating that numerical results are in good agreement with the experimental results. The failure strengths and strains in the tensile and in-plane shear FE models with different mesh sizes are summarised in Table 4. The FE results show a good converge as the differences of failure strength and strains predicted by different mesh sizes are within 1%.

5. Discussion

Studies [6,15] reported that damage onset in the tows could be captured by the continuum damage mechanics (CDM) approach, but the damage propagation was predicted incorrectly. The built-in material model 54 for composite damage in LS-DYNA was based on the CDM approach with the maximum strain or stress criteria. Matrix cracking could extend through the entire 90° layers, using the stress degradation in the material model. However, an experimental study [6] characterised different types of matrix cracking in the transverse tows of NCF composites and clarified that the through-thickness cracks were only one of them. Studies [6,15] suggested measuring the density of matrix cracks to predict the degradation of modulus and Poisson's ratio or inserting discrete cracks into the RUC models, which was not applicable for this study. Nevertheless, the difference between tensile strengths predicted by the meso RUC models with and without stress degradation was within 0.2 % in this study. Therefore, using the CDM approach to model the tows in this study was feasible because matrix cracking caused a slight influence on the prediction of the overall tensile strength of the biaxial NCF composite.

The influence of mesh size on the meso RUC model was discussed. In the preceding RUC analysis, the mesh of the meso RUC models was 0.0855 × 0.0855 × 0.075 mm^3. As shown in Fig. 14 (a), the meso RUC models with different mesh sizes are created to model the damage behaviour of the tensile specimen with layup A, where 'm' and 'n' represent the number of elements in the Y- (longitudinal) and Z- (thickness) directions, respectively. Due to symmetry, only half of the surface 0° tows in the full-thickness RUC models are presented. Fig. 14 (a) presents the local X- stress distributions at the applied strain ε = 0.01. The damage initiation and propagation in the surface 0° tow are associated with the maximum X-stress (red region). The tensile strengths predicted by the models with different meshes are depicted in Fig. 14 (b). Fig. 14 (a) shows that when more than one element layer is stacked in the thickness direction, the damage is localised in the element layer below the surface element layer. In addition, Fig. 14 (b) shows the converged results of the predicted tensile strengths (within 10% of the mean test result) except for the strength of the finest mesh size (m = 20, n = 4). This might be caused by the localisation when using the local damage model, leading to the mesh-dependence problem.

Some studies [40–42] mentioned the mesh-dependence problem due to progressive damage models used for modelling the tow in textile composites. Fracture energy [43,44] and non-local damage model [45,46] have been implemented in progressive damage models or homogenisation algorithms to avoid mesh dependency. However, the method of fracture energy might not eliminate the pathological damage localisation as it mainly controlled damage evolution rather than initiation. Thus, a non-local damage model was expected to be a solution to minimise the mesh-dependence problem in future work.

In this study, avoiding overly refined mesh size was the simplest scheme to eliminate pathological damage localisation. The scheme of stacking two-element layers in the tow thickness direction was adopted because it could reasonably account for the bending behaviour of tows and the debonding of surface tows. Although decreasing the mesh size in the in-plane direction should not obviously influence the predicted result, the calculation time could be increased. Besides, the progressive damage model was developed for the macroscopic damage of unidirectional laminates, which might not correctly predict the in-situ strength of a localised material point. Future studies could validate the feasibility of using the laminate damage models to model the *meso*-scale tows under more complex loadings.

Fig. 15 compares the axial strains ε_x of the DIC measurements and the meso RUC model with diamond-shaped resin-rich areas at the applied tensile strain ε = 0.01. Fig. 15 (a) presents the strain map ε_x within the gauge length of the tensile specimen, with a facet size of 17 pixels × 17 pixels and a point distance of 15 pixels. Fig. 15 (b) compares the local strain maps ε_x, corresponding to the small window marked in Fig. 15 (a), with different facet sizes and point distances. The strain distributions along the sections of the strain maps and the meso RUC model are compared, as shown in Fig. 15 (c).

Fig. 15 (b) shows that using the smaller facet size and point distance can increase the maximum and minimum strains in the local strain maps. However, the FE model has more obvious peaks and valleys than

the DIC measurements, while the strain distributions measured by DIC are close to the averaged value of the FE result. It should be noted that the strains measured by DIC represented the surface deformation of the tensile specimen consisting of 16-layer NCF plies, while the strains of the meso RUC model represented the deformation of the interior layers. The relevant study [47] indicated that the nesting of layers in textile composite could smooth the strain profile and reduce the resolution. Therefore, the choice of the specimen thickness could be a major reason for the low resolution. However, the strain maps measured from the thin specimen could not represent the actual values of an interior layer of a thicker specimen. The other way of improving resolution was to reduce the measured volume and focus on a local area of the specimen. However, a large number of local strain maps were required to avoid local effects, leading to a tremendous amount of experimental work. Despite the low resolutions of DIC measurements, the distance between the major stress concentrations is about 7.5 mm, corresponding to the distance between the neighbouring diamond-shaped resin-rich areas, as shown in Fig. 15 (c). The good agreement indicates that meso FE modelling is a potential tool to investigate the actual strain distributions of the internal layers.

The novel 3D meso RUC model offered a virtual testing framework for NCF composites, which could well capture the in-situ strengths. The in-plane shear strength was predicted as 117 MPa by the meso RUC models with the out-of-phase structures S1 and S2 under a pure-shear boundary condition. The result of in-plane shear strength 117 MPa was used as a material input of the macroscopical damage model in the FE modelling of in-plane shear coupon tests. The predicted results were in good agreement with the experiment result with the in-plane shear strength of 98 MPa. Thus, the in-plane tests based on the standard ASTM D3518 underestimated the actual in-plane shear strengths. Besides, the lower tensile strength of the specimen with layup $[0/90]_{4s}$ was influenced by the bending effects of surface 0° tows. The lower tensile strength could not represent the tensile strength of the NCF composites using off-axis plies as the surface layers. Further study regarding the biaxial NCF composites under compression and impact loadings can be conducted to validate the multiscale FE modelling.

6. Conclusion

This study proposed novel 3D RUC models of biaxial NCF composites to investigate the critical factors influencing their uniaxial tensile and in-plane shear strengths. A systematic parameter study was conducted based on the meso RUC models, including layups, the placement of transverse tows, tow waviness, delamination, and diamond-shaped resin-rich areas.

The predicted results of meso RUC models provided insight into the critical factors influencing the in-plane strengths of the biaxial NCF composite. Due to layer shifting existing in NCF composite, the out-of-phase placed tows were more common than the in-phase placed tows. The out-of-phase placement of tows in NCF composites was found to have different influences on the tensile and in-plane shear strengths. The out-of-phase placed tows could be unsymmetric about the middle plane of NCF composites, leading to the bending effects of surface 0° tows during uniaxial tension. Therefore, the layup $[0/90]_{4s}$ had a lower tensile strength than the layup $[90/0]_{4s}$. However, when the meso RUC models were under in-plane shear, the dispersion of resin-rich areas caused by the out-of-phase placed tows reduced stress concentrations. Therefore, the out-of-phase placement of tows in NCF composites could lead to a reduction in the tensile strength of the layup $[0/90]_{4s}$ but an increase in the in-plane shear strength. In practical application, the off-axis plies should be placed as the surface layers to avoid the debonding of surface 0° tows during tensile loading.

Similarly, tow waviness in NCF composites had different influences on the in-plane strengths. Under uniaxial tension, increasing tow waviness led to higher bending stresses, reducing the tensile strength. Under in-plane shear, increasing tow waviness reduced stress concentrations caused by resin-rich areas, enhancing the in-plane shear strength. Therefore, the reduced tensile strength was a major drawback for NCF composites in structural application. In future work, the influence of tow waviness on the compressive strength should be investigated. Interlaminar delamination was not involved in the damage process of uniaxial tension and in-plane shear. Therefore, the interlaminar shear strength did not significantly influence the uniaxial tensile and in-plane shear strengths, indicating that the improved interlaminar resistance by stitching yarn may not enhance tensile and in-plane shear strengths. The presence of diamond-shaped resin-rich areas in NCF composites, associated with the diameter of stitching yarns [13], caused the degradation of uniaxial tensile and in-plane shear strengths. However, the decrease in the tensile strength was significantly higher than in the in-plane shear strength. Therefore, the diameter of stitching yarns and tow waviness were major factors controlling the tensile strength of NCF composites.

The homogenised results obtained from the meso RUC models were used as material inputs in the macroscopic damage model of biaxial NCF composites, developed by Iannucci et al. [18–20] as a UMAT in LS-DYNA. The UMAT was used in the FE modelling of biaxial NCF composites in uniaxial tension and in-plane shear coupon tests. The numerical modelling results were in good agreement with the experimental results. Therefore, the micro RVE model, the novel 3D meso RUC models and the macroscopical damage model comprised a virtual testing framework, providing an insight into the critical parameters influencing the mechanical properties of NCF composites. The multiscale framework improved the numerical methods of analysing NCF composites and contributed to a potential numerical tool for the application of NCF composites.

CRediT authorship contribution statement

Han Yin: Conceptualization, Methodology, Software, Validation, Investigation, Writing – original draft, Visualization. **Qianqian Li:** Writing – review & editing, Supervision. **Lorenzo Iannucci:** Conceptualization, Methodology, Resources, Writing – review & editing, Supervision.

Declaration of Competing Interest

The authors declare that they have no known competing financial interests or personal relationships that could have appeared to influence the work reported in this paper.

Acknowledgements

This research did not receive any specific grant from funding agencies in the public, commercial, or not-for-profit sectors. The authors would like to acknowledge Cristex for the supply of non-crimp fabrics, and Solvay for the supply of MTM57 resin films. The authors also would like to acknowledge Dr Frank Gommer, Mr Gary Senior and Mr Jon Cole for the help of manufacture, and Mr Joseph Meggyesi and Mr Keith Wolstenholme for the help of mechanical testing. The authors also would like to acknowledge Mr Zhenghao Zhang for the help of taking photos of test specimens.

Appendix A. Micromechanical FE modelling

A.1. Model set up

Micro RVE models were created to investigate the mechanical behaviours of tows in the NCF composites. A micro RVE model was composed of fibre and matrix. The transverse tensile and in-plane shear strengths of the tows were predicted by the micro RVE models. As shown in Fig. A1 (a) and (b), micro RVE models are constructed with 30 carbon fibre inclusions (V_f = 74%) but different fibre distribution patterns. The relevant studies [37,48,49] have demonstrated that 30 fibre inclusions were enough to capture the transverse mechanical behaviours of unidirectional laminates. Eight-node hexahedral solid elements are adopted in micro RVE models, and their FE discretisation is presented in Fig. A1 (a) and (b). As shown in Fig. A1 (c), two thin element layers are stacked in the longitudinal direction (X-axis) of the micro RVE model because the deformation gradient along the longitudinal direction can be negligible under transverse tensile or in-plane shear loadings [37]. In total, approximately 18,800 elements are employed in the micro RVE models. The geometries of the micro RVE models are assumed to be periodic at the Z-Y plane, so the nodes on the opposite surfaces can be matched. PBCs were applied to the opposite surfaces of the RVE models following the method proposed in the relevant study [27].

Fig. A1 (d) shows that the cohesive surface can be used to model the fibre–matrix debonding. Interfacial normal and shear strengths were equal $t_n^0 = t_s^0$ for simplification. The interfacial strengths 40, 80, and 120 MPa were labelled 'S40', 'S80', and 'S120' to investigate the influence of interfacial strength on the mechanical properties of tow. Fibres and matrix were perfectly bonded in the model labelled as 'S∞'. Interfacial fracture toughness was assumed to be 100 J/m^2. The fracture toughness was demonstrated to dominate the maximum displacement of debonding [38], which was not in the interest of this study. The penalty stiffness was set as K = 10^8 GPa/m for computational stability [37,48,49].

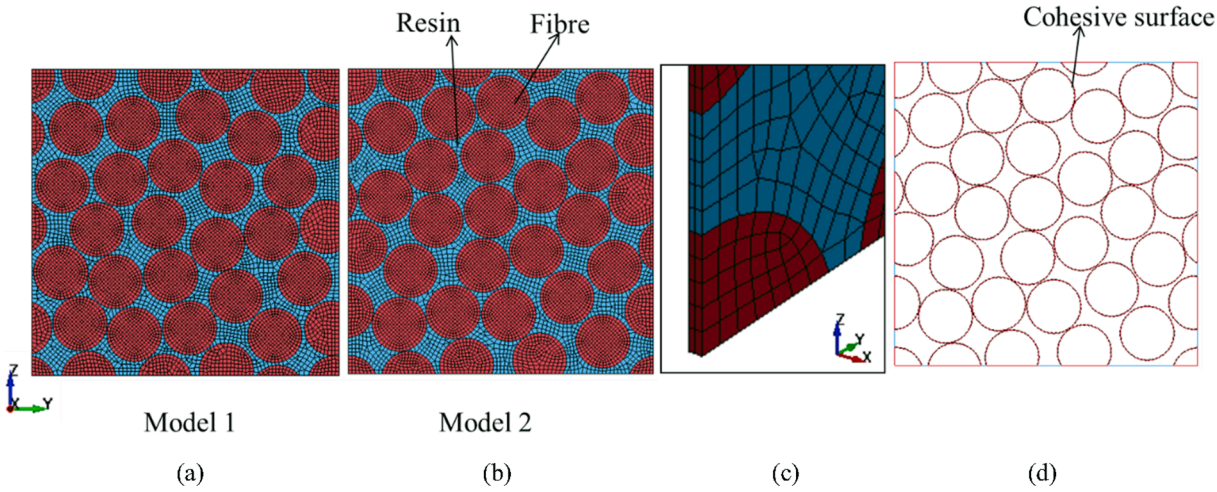

Fig. A1. Micro RVE model set-up: (a)-(b) FE discretisation of the micro RVE models with 30 fibres and the fibre volume fraction of 74%; (c) Illustration of element stacks in the X-direction; (d) Illustration of cohesive surface to model fibre–matrix debonding.

A.2. Material model

The carbon fibre T700 in the micro RVE models was assumed to the linear elastic because fibre damage was not involved in the damage process of transverse tension and in-plane shear of biaxial NCF composites. The built-in material model in LS-DYNA for the Mohr-Coulomb yield criterion was employed to model the MTM57 resin. The mechanical parameters of fibre and matrix are tabulated in Table A1. The parameters c (cohesion yield stress) and ϕ (angle of internal friction) in the Mohr-Coulomb yield criterion were set to be 52 MPa and 15°, respectively, based on the relevant studies [37,38].

Table A1
Mechanical properties of carbon fibre T700 and resin MTM57.

Elastic properties	Carbon fibre (T700)	Resin (MTM57)
$E_{11}(GPa)$	230 [a]	3.35[c]
$E_{22(33)}(GPa)$	28[b]	
$G_{12(13)}(GPa)$	24[b]	1.24[c]
$G_{23}(GPa)$	7.2 [b]	
$\nu_{12(13)}$	0.23[b]	0.35[c]
ν_{23}	0.33[b]	

[a] TORAY datasheet.
[b] Carbon fibre properties from the literature[38].
[c] SOLVAY datasheet.

A.3. Transverse tension

At the initial stage, fibre and matrix showed linear-elastic behaviours. When the interfacial stresses exceeded the interfacial normal strength t_n^0, fibre–matrix debonding occurred rapidly. A transverse crack develops throughout the RVE model, as shown in Fig. A2 (a) and (b). Matrix yielding occurs at the region of the transverse crack, which controls the maximum strength of the RVE model.

The transverse tensile stress σ was determined by the reaction force divided by the total area in the Y-direction, while the strain ε was determined by the elongation divided by the total length in the Y-direction. Fig. A2 (c) shows stress–strain curves of the models with different fibre volume fractions, interfacial strengths, and fibre distribution patterns. Fig. A2 (d) presents a detailed analysis regarding the influences of fibre volume fraction on the strength and modulus, where all the models are assumed to have the interfacial strength of 80 MPa.

As shown in Fig. A2 (c), the overall strength of the RVE models increases with the interfacial strength. The perfect bonded model was failed by local matrix damages. The different fibre distribution patterns could not influence the stress–strain curves. Fig. A2 (d) indicates that the influence of fibre volume fraction on the transverse tensile strength is minor as the difference of the strengths is within 3%. However, the transverse tensile modulus increases linearly with the fibre volume fraction. Therefore, the overall strength of the RVE model under transverse tension was mainly controlled by the interfacial strength.

Extensive experimental works [50–52] have demonstrated the fracture surface in carbon fibre/epoxy under transverse tensile loading develops at the fibre–matrix interface, indicating the interfacial strength is usually lower than the matrix strength. The matrix in the region of stress concentrations failed after interfacial debonding, which could not influence the transverse tensile strength. In addition, the plastic failure strains of the matrix are strongly influenced by tri-axiality [53], posing a challenge to find an appropriate material model in LS-DYNA to predict the failure of the matrix in a complex strain state. The material model of the meso RUC model only required the input of elastic properties and strengths predicted by the micro RVE models. Thus, the matrix failure was not considered in this micro RVE analysis.

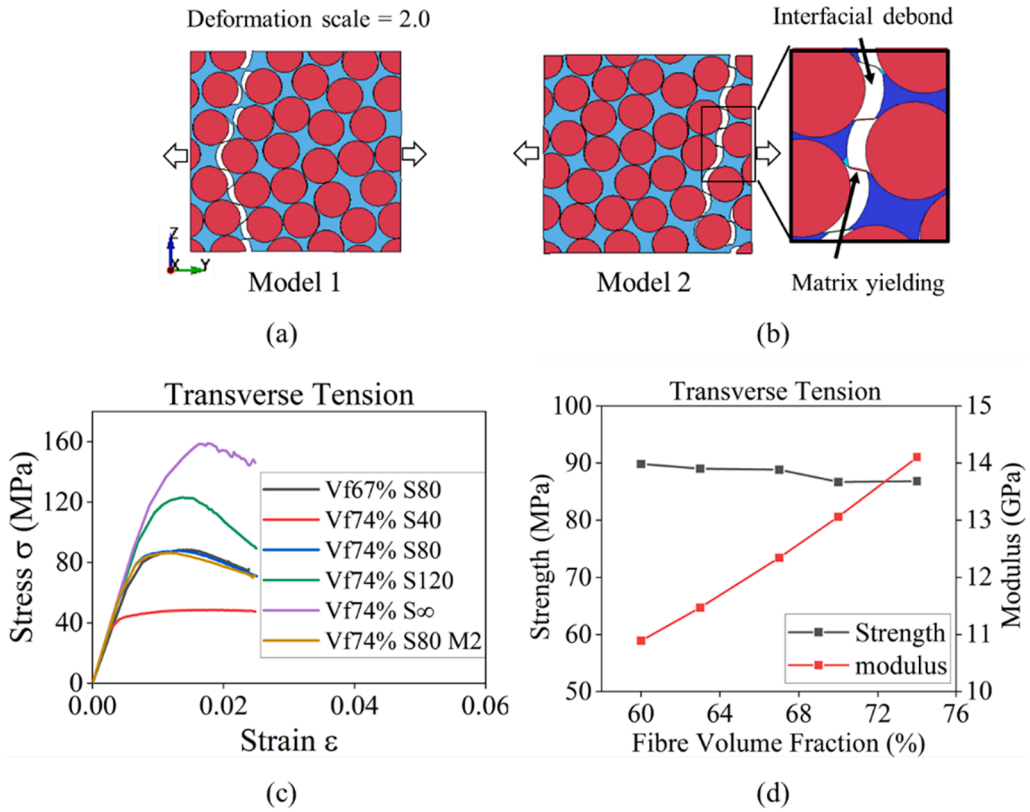

Fig. A2. Micro RVE models subject to transverse tension: (a)-(b) An interfacial crack develops through the total thickness of micro RVE models; (c) Stress–strain curves of micro RVE models with different fibre volume fraction, interfacial strength, and fibre distribution pattern; (d) Influence of fibre volume fraction on the strength and modulus.

A.4. In-plane shear

Shear strains $\varepsilon_{12}\|$ and $\varepsilon_{12}^{\perp}$ were imposed on the X and Y surfaces of the micro RVE models to produce shear stresses $\tau_{12}\|$ and $\tau_{12}^{\perp}$. The symbols '$\|$' and '$\perp$' represented the shear deformations parallel and perpendicular to the fibres, respectively. Shear stresses $\tau_{12}\|$ and $\tau_{12}^{\perp}$ were determined by the total shear forces on the X and Y surfaces of the RVE models divided by the corresponding surface areas, respectively. The average shear stress in the micro RVE model was calculated as $(\tau_{12}\| + \tau_{12}^{\perp})/2$, while the total shear strain γ was the sum of the shear strains $\varepsilon_{12}\|$ and $\varepsilon_{12}^{\perp}$.

Fig. A3 (a) shows the stress–strain curves of the micro RVE models before $\gamma = 0.2$. Based on the relevant study [37], the shear stress $\tau_{12}\|$ caused by matrix plastic deformation was equivalent to the shear yielding strength of the matrix. The shear stress $\tau_{12}^{\perp}$ caused by fibre rotation accounted for the increased curvature of the shear stress–strain curves. Therefore, the shear strain $\varepsilon_{12}^{\perp}$ was imposed on the micro RVE model based on the slope of experimental stress–strain curves. Fig. A3 (b) presents a detailed analysis regarding the influences of fibre volume fraction on the strength and modulus, where all the models are assumed to have the interfacial strength of 80 MPa.

The matrix plastic deformations in a micro RVE model at different applied shear strains are presented in Fig. A3 (c). Similar to the previous study [37], the yield point I in the stress–strain curves corresponds to the generation of the matrix yield band perpendicular to the X-Y plane. During stage II, more parallel matrix yield bands are generated. Besides, fibres rotate during stage II to accommodate the increased shear strain, corresponding to the linear hardening region in the in-plane shear curve [37]. Interfacial stresses reach the interfacial shear strength t_s^0 at stage III, determining the overall shear strength. Therefore, in the stress–strain curves of Fig. A3 (a), the increase of interfacial shear strength improves the in-plane shear strength. Besides, fibre volume fraction and fibre distribution pattern could not cause significant influences on the stress–strain curves because the in-plane shear behaviour is matrix-dominated. According to Fig. A3 (b), the in-plane shear strength is improved by 6% when the fibre volume fraction increases from 60% to 74%. The shear modulus increases linearly with the fibre volume fraction, similar to the trend found in the modulus of the micro RVE model under transverse tension.

The stress–strain curve of the micro RVE model with the interfacial strength of 100 MPa was used as an input in meso FE modelling, providing a good fit with the experiment result. The interfacial shear strength of 100 MPa has been proved to be an average value of the carbon fibre reinforced epoxy resin laminates [37]. The good match validated the feasibility of the micro RVE models.

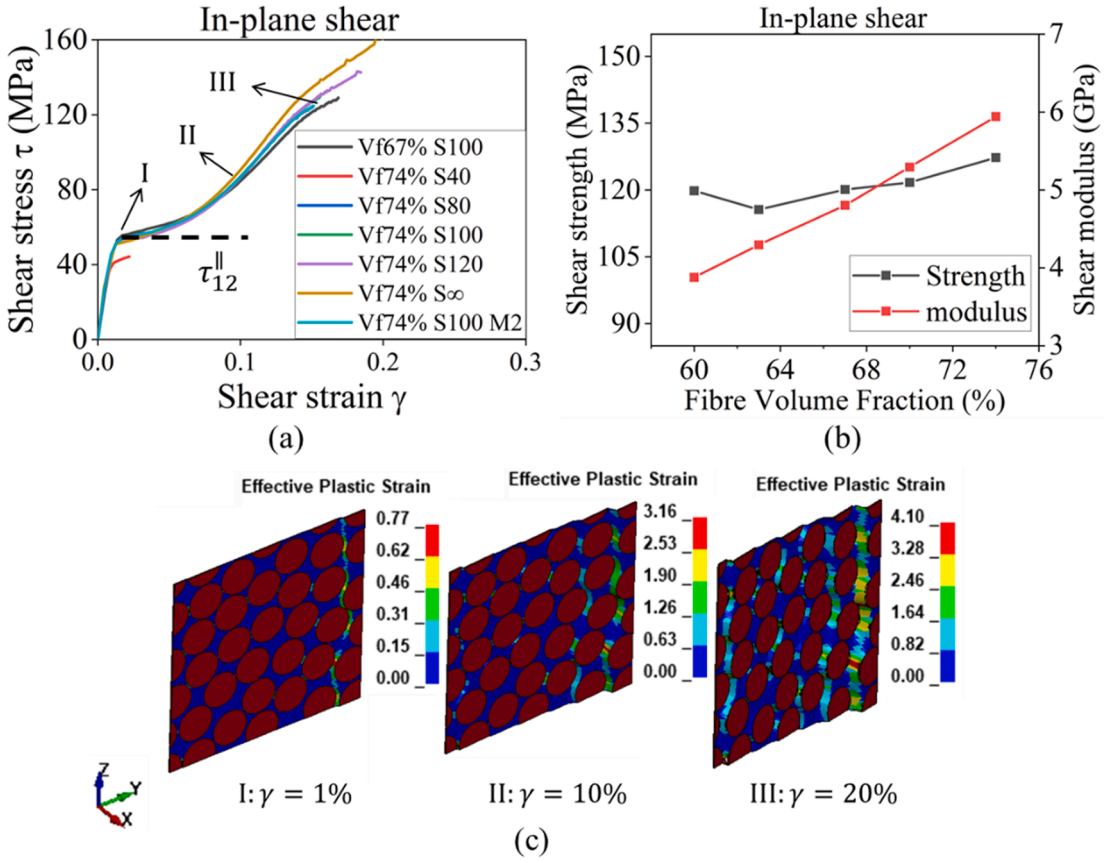

Fig. A3. Micro RVE models subject to in-plane shear: (a) Shear stress–strain curves of micro RVE models with different fibre volume fraction, interfacial strength, and fibre distribution pattern; (b) Influence of fibre volume fraction on the strength and modulus of the micro RVE models; (c) Matrix plastic deformation in the micro RVE model with $V_f = 74\%$ at the applied shear strains $\gamma = 1\%$, 10% and 20%.

A.5. Elastic properties of tow

The method of solving elastic constants from the compliance matrix of an RVE model was introduced in a previous study [27]. For an orthotropic material, nine independent material constants in the stiffness matrix needed to be determined. All the material properties were assumed to be elastic, and the interface between fibre and matrix was perfectly bonded under a small strain. The elastic properties of the tow with the fibre volume fraction of 74% predicted by models with different element numbers are listed in Table A2. The error caused by the different sizes is within 1%, indicating that the homogenised elastic properties are not sensitive to the mesh size. The elastic properties precited by the finer mesh were used in the meso FE modelling of NCF composites.

Table A2
Elastic constants of the tow with the fibre volume fraction of 74%.

Elastic properties	E_{11} (GPa)	$E_{22(33)}$ (GPa)	$G_{12(13)}$ (GPa)	G_{23} (GPa)	$\upsilon_{12(13)}$	υ_{23}
89,345 elements	169.2	11.5	6.3	3.9	0.29	0.42
52,745 elements	168.2	11.4	6.2	3.9	0.29	0.42
37,675 elements	168.2	11.4	6.2	3.9	0.29	0.42

Appendix B. The DIC measurement uncertainty

According to relevant studies [54], the noise present within the DIC technique may be associated with measurement uncertainty. The DIC noise includes image noise, illumination variations, speckle patterns, etc. The strains in the X- and Y-directions of the unstressed specimen are shown in Fig. B1 to characterise the background noise. The strain histograms show that the distributions of measurement error are close to Gaussian. The mean values are 0, corresponding to the known zero strain. The maximum and minimum errors are about 0.1% and −0.1%, respectively. The error was caused by noise present within the DIC technique, which also existed in the stressed specimen. As the noise did not influence the mean value, the measured averaged strains could still reflect the overall deformation of the specimen. Also, the error caused by the noise was small, leading to a minor influence on the strain results.

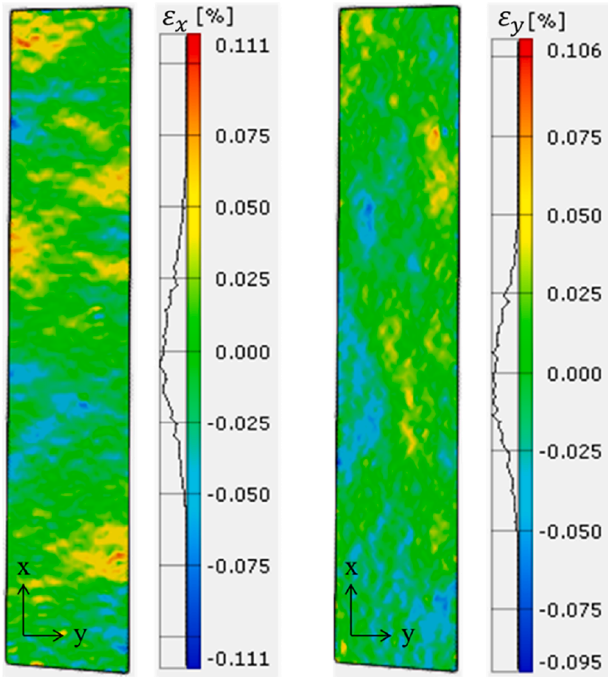

Fig. B1. Measured strain fields of the unstressed specimen in the X- and Y-directions.

References

[1] Bibo GA, Hogg PJ, Kemp M. Mechanical characterisation of glass- and carbon-fibre-reinforced composites made with non-crimp fabrics. Compos Sci Technol 1997;57(9-10):1221–41.
[2] Lomov SV. Non-crimp fabric composites: manufacturing, properties and applications. Elsevier; 2011.
[3] Budwal N, Kasper K, Goering J, Ward C. Flexible low-cost tooling solutions for a one-shot resin infusion of a 3D woven and multi-textile preform. Procedia Manuf 2020;51:856–63.
[4] González A, Graciani E, París F. Prediction of in-plane stiffness properties of non-crimp fabric laminates by means of 3D finite element analysis. Compos Sci Technol 2008;68(1):121–31. https://doi.org/10.1016/j.compscitech.2007.05.026.
[5] Mikhaluk DS, Truong TC, Borovkov AI, Lomov SV, Verpoest I. Experimental observations and finite element modelling of damage initiation and evolution in

carbon/epoxy non-crimp fabric composites. Eng Fract Mech 2008;75(9):2751–66. https://doi.org/10.1016/j.engfracmech.2007.03.010.
[6] Edgren F, Mattsson D, Asp LE, Varna J. Formation of damage and its effects on non-crimp fabric reinforced composites loaded in tension. Compos Sci Technol 2004;64(5):675–92. https://doi.org/10.1016/S0266-3538(03)00292-6.
[7] Mattsson D, Joffe R, Varna J. Damage in NCF composites under tension: Effect of layer stacking sequence. Eng Fract Mech 2008;75(9):2666–82. https://doi.org/10.1016/j.engfracmech.2007.03.014.
[8] Drapier S, Wisnom MR. Finite-element investigation of the compressive strength of non-crimp-fabric-based composites. Compos Sci Technol 1999;59(8):1287–97. https://doi.org/10.1016/S0266-3538(98)00165-1.
[9] Mouritz AP, Cox BN. A mechanistic approach to the properties of stitched laminates. Compos Part A Appl Sci Manuf 2000;31(1):1–27. https://doi.org/10.1016/S1359-835X(99)00056-1.
[10] Edgren F, Asp LE. Approximate analytical constitutive model for non-crimp fabric composites. Compos Part A Appl Sci Manuf 2005;36(2):173–81.
[11] Beier U, Fischer F, Sandler JKW, Altstädt V, Weimer C, Buchs W. Mechanical performance of carbon fibre-reinforced composites based on stitched preforms. Compos Part A Appl Sci Manuf 2007;38(7):1655–63.
[12] Hes H, Roth Y, Himmel N. Elastic constants estimation of stitched NCF CFRP laminates based on a finite element unit-cell model. Compos Sci Technol 2007;67(6):1081–95. https://doi.org/10.1016/j.compscitech.2006.05.024.
[13] Heß H, Himmel N. Structurally stitched NCF CFRP laminates. Part 1: experimental characterization of in-plane and out-of-plane properties. Compos Sci Technol 2011;71(5):549–68. https://doi.org/10.1016/j.compscitech.2010.11.012.
[14] Drapier S, Wisnom MR. A finite-element investigation of the interlaminar shear behaviour of non-crimp-fabric-based composites. Compos Sci Technol 1999;59(16):2351–62. https://doi.org/10.1016/S0266-3538(99)00091-3.
[15] Doitrand A, Fagiano C, Chiaruttini V, Leroy FH, Mavel A, Hirsekorn M. Experimental characterization and numerical modeling of damage at the mesoscopic scale of woven polymer matrix composites under quasi-static tensile loading. Compos Sci Technol 2015;119:1–11. https://doi.org/10.1016/j.compscitech.2015.09.015.
[16] Doitrand A, Fagiano C, Leroy FH, Mavel A, Hirsekorn M. On the influence of fabric layer shifts on the strain distributions in a multi-layer woven composite. Compos Struct 2016;145:15–25. https://doi.org/10.1016/j.compstruct.2016.02.054.
[17] Ivanov D, Ivanov S, Lomov S, Verpoest I. Strain mapping analysis of textile composites. Opt Lasers Eng 2009;47(3-4):360–70.
[18] Iannucci L. Progressive failure modelling of woven carbon composite under impact. Int J Impact Eng 2006;32(6):1013–43. https://doi.org/10.1016/j.ijimpeng.2004.08.006.
[19] Iannucci L, Ankersen J. An energy based damage model for thin laminated composites. Compos Sci Technol 2006;66(7-8):934–51. https://doi.org/10.1016/j.compscitech.2005.07.033.
[20] Iannucci L, Willows ML. An energy based damage mechanics approach to modelling impact onto woven composite materials—Part I: numerical models. Compos Part A Appl Sci Manuf 2006;37(11):2041–56.
[21] ASTM International. D3039/D3039M-17 standard test method for tensile properties of polymer matrix. Compos Mater 2017. https://doi.org/10.1520/D3039_D3039M-17.
[22] ASTM International. D3518/D3518M-18 Standard Test Method for In-Plane Shear Response of Polymer Matrix Composite Materials by Tensile Test of a ±45° Laminate; 2018. https://doi.org/10.1520/D3518_D3518M-18.
[23] FALCOM. Failure, performance and processing prediction for enhanced design with non-crimp-fabric composites. EU-Project; n.d.
[24] Bader MG. Tensile strength of uniaxial composites. Sci Eng Compos Mater 1988;1:1–12. https://doi.org/10.1515/SECM.1988.1.1.1.
[25] Adams DF. Test methods for mechanical properties. Compr Compos Mater 2000:113–48. https://doi.org/10.1016/B0-08-042993-9/00037-1.
[26] Zhao LG, Warrior NA, Long AC. Finite element modelling of damage progression in non-crimp fabric reinforced composites. Compos Sci Technol 2006;66(1):36–50. https://doi.org/10.1016/j.compscitech.2005.06.002.
[27] Xia Z, Zhang Y, Ellyin F. A unified periodical boundary conditions for representative volume elements of composites and applications. Int J Solids Struct 2003;40(8):1907–21. https://doi.org/10.1016/S0020-7683(03)00024-6.
[28] Tessitore N, Riccio A. A novel FEM model for biaxial non-crimp fabric composite materials under tension. Comput Struct 2006;84(19-20):1200–7. https://doi.org/10.1016/j.compstruc.2006.01.024.
[29] Heimbs S, Heller S, Middendorf P, Hähnel F, Weiße J. Low velocity impact on CFRP plates with compressive preload: Test and modelling. Int J Impact Eng 2009;36(10-11):1182–93.
[30] Xiao X, Botkin ME, Johnson NL. Axial crush simulation of braided carbon tubes using MAT58 in LS-DYNA. Thin-Walled Struct 2009;47(6-7):740–9. https://doi.org/10.1016/j.tws.2008.12.004.
[31] Kempesis D, Iannucci L, Rosso SD, Curtis PT, Pope D, Duke PW. A representative volume element model for ultra-high-molecular-weight-polyethylene composites. Compos Struct 2021;262:113609. https://doi.org/10.1016/j.compstruct.2021.113609.
[32] Hallquist JO. LS-DYNA® Keyword User's Manual Volume II Material Models. Livermore, California, USA; 2013.
[33] Turon A, Dávila CG, Camanho PP, Costa J. An engineering solution for mesh size effects in the simulation of delamination using cohesive zone models. Eng Fract Mech 2007;74(10):1665–82. https://doi.org/10.1016/j.engfracmech.2006.08.025.
[34] Zou Z, Reid SR, Li S, Soden PD. Modelling interlaminar and intralaminar damage in filament-wound pipes under quasi-static indentation. J Compos Mater 2002;36(4):477–99. https://doi.org/10.1177/0021998302036004539.
[35] Doitrand A, Estevez R, Leguillon D. Comparison between cohesive zone and coupled criterion modeling of crack initiation in rhombus hole specimens under quasi-static compression. Theor Appl Fract Mech 2019;99:51–9. https://doi.org/10.1016/j.tafmec.2018.11.007.
[36] Truong TC, Vettori M, Lomov S, Verpoest I. Carbon composites based on multi-axial multi-ply stitched preforms. Part 4. Mechanical properties of composites and damage observation. Compos Part A Appl Sci Manuf 2005;36(9):1207–21.
[37] Totry E, Molina-Aldareguía JM, González C, LLorca J. Effect of fiber, matrix and interface properties on the in-plane shear deformation of carbon-fiber reinforced composites. Compos Sci Technol 2010;70:970–80. https://doi.org/10.1016/J.COMPSCITECH.2010.02.014.
[38] Vaughan TJ, McCarthy CT. Micromechanical modelling of the transverse damage behaviour in fibre reinforced composites. Compos Sci Technol 2011;71(3):388–96. https://doi.org/10.1016/j.compscitech.2010.12.006.
[39] Gigliotti L, Pinho ST. Translaminar fracture toughness of NCF composites with multiaxial blankets. Mater Des 2016;94:410–6. https://doi.org/10.1016/j.matdes.2015.12.167.
[40] Lomov S, Ivanov D, Verpoest I, Zako M, Kurashiki T, Nakai H, et al. Meso-FE modelling of textile composites: Road map, data flow and algorithms. Compos Sci Technol 2007;67(9):1870–91. https://doi.org/10.1016/j.compscitech.2006.10.017.
[41] Whitcomb J, Srirengan K. Effect of various approximations on predicted progressive failure in plain weave composites. Compos Struct 1996;34(1):13–20. https://doi.org/10.1016/0263-8223(95)00125-5.
[42] Bednarcyk BA, Stier B, Simon JW, Reese S, Pineda EJ. Meso- and micro-scale modeling of damage in plain weave composites. Compos Struct 2015;121:258–70. https://doi.org/10.1016/j.compstruct.2014.11.013.
[43] Ernst G, Vogler M, Hühne C, Rolfes R. Multiscale progressive failure analysis of textile composites. Compos Sci Technol 2010;70(1):61–72. https://doi.org/10.1016/j.compscitech.2009.09.006.
[44] Wang L, Wu J, Chen C, Zheng C, Li B, Joshi SC, et al. Progressive failure analysis of 2D woven composites at the meso-micro scale. Compos Struct 2017;178:395–405.
[45] Zhang X, O'Brien DJ, Ghosh S. Parametrically homogenized continuum damage mechanics (PHCDM) models for composites from micromechanical analysis. Comput Methods Appl Mech Eng 2019;346:456–85. https://doi.org/10.1016/J.CMA.2018.12.005.
[46] Liu Z, Fleming M, Liu WK. Microstructural material database for self-consistent clustering analysis of elastoplastic strain softening materials. Comput Methods Appl Mech Eng 2018;330:547–77. https://doi.org/10.1016/j.cma.2017.11.005.
[47] Lomov SV, Ivanov DS, Verpoest I, Zako M, Kurashiki T, Nakai H, et al. Full-field strain measurements for validation of meso-FE analysis of textile composites. Compos Part A Appl Sci Manuf 2008;39(8):1218–31.
[48] Yang L, Yan Y, Liu Y, Ran Z. Microscopic failure mechanisms of fiber-reinforced polymer composites under transverse tension and compression. Compos Sci Technol 2012;72(15):1818–25. https://doi.org/10.1016/j.compscitech.2012.08.001.
[49] González C, LLorca J. Mechanical behavior of unidirectional fiber-reinforced polymers under transverse compression: Microscopic mechanisms and modeling. Compos Sci Technol 2007;67:2795–806. https://doi.org/10.1016/j.compscitech.2007.02.001.
[50] Hobbiebrunken T, Hojo M, Adachi T, De Jong C, Fiedler B. Evaluation of interfacial strength in CF/epoxies using FEM and in-situ experiments. Compos Part A Appl Sci Manuf 2006;37(12):2248–56.
[51] Hughes JDH. The carbon fibre/epoxy interface-A review. Compos Sci Technol 1991;41(1):13–45. https://doi.org/10.1016/0266-3538(91)90050-Y.
[52] Gamstedt EK, Sjögren BA. Micromechanisms in tension-compression fatigue of composite laminates containing transverse plies. Compos Sci Technol 1999;59(2):167–78. https://doi.org/10.1016/S0266-3538(98)00061-X.
[53] Fiedler B, Hojo M, Ochiai S, Schulte K, Ando M. Failure behavior of an epoxy matrix under different kinds of static loading. Compos Sci Technol 2001;61(11):1615–24. https://doi.org/10.1016/S0266-3538(01)00057-4.
[54] He T, Liu L, Makeev A. Uncertainty analysis in composite material properties characterization using digital image correlation and finite element model updating. Compos Struct 2018;184:337–51. https://doi.org/10.1016/J.COMPSTRUCT.2017.10.009.